



**UNIVERSIDAD DE INVESTIGACIÓN DE
TECNOLOGÍA EXPERIMENTAL
YACHAY**

Escuela de Ciencias Físicas y Nanotecnología

**TÍTULO: Structure of Shocked Gas in Interstellar
Cloud-Cloud Collisions.**

Trabajo de integración curricular presentado como
requisito para la obtención
del título de Físico.

Autor:

Navarrete Piedra Pablo Sebastián

Tutor:

PhD. – Banda Wladimir

Urcuquí, noviembre 2023

AUTORÍA

Yo, **Navarrete Piedra Pablo Sebastián**, con cédula de identidad 1004352520, declaro que las ideas, juicios, valoraciones, interpretaciones, consultas bibliográficas, definiciones y conceptualizaciones expuestas en el presente trabajo; así cómo, los procedimientos y herramientas utilizadas en la investigación, son de absoluta responsabilidad de el/la autora (a) del trabajo de integración curricular. Así mismo, me acojo a los reglamentos internos de la Universidad de Investigación de Tecnología Experimental Yachay.

Urcuquí, noviembre 2023.

Navarrete Piedra Pablo Sebastián

CI: 1004352500

AUTORIZACIÓN DE PUBLICACIÓN

Yo, **Navarrete Piedra Pablo Sebastián**, con cédula de identidad 1004352520, cedo a la Universidad de Investigación de Tecnología Experimental Yachay, los derechos de publicación de la presente obra, sin que deba haber un reconocimiento económico por este concepto. Declaro además que el texto del presente trabajo de titulación no podrá ser cedido a ninguna empresa editorial para su publicación u otros fines, sin contar previamente con la autorización escrita de la Universidad.

Asimismo, autorizo a la Universidad que realice la digitalización y publicación de este trabajo de integración curricular en el repositorio virtual, de conformidad a lo dispuesto en el Art. 144 de la Ley Orgánica de Educación Superior

Urququí, noviembre 2023.

Navarrete Piedra Pablo Sebastián
CI: 1004352500

Dedication

I dedicate this work to all my family. Especially to my dad and mom, Pablo and Humbertina, for their wisdom, love, and support in encouraging me to pursue my dreams. To my siblings Mari, Gaby, and Josue for their unconditional friendship and for always staying with me, even the distance. Finally, to my niece and nephews Sarita, Francis, and Joaquin.

Pablo Sebastián Navarrete Piedra

Acknowledgements

To everyone who stood with me during my academic journey. To my family for their support, patience, and kindness. I am deeply grateful to my parents. Their love has been my foundation and motivation during my college years. I owe my immense gratitude to my advisor, Wladimir, for their guidance and advice.

The author acknowledges the Gauss Centre for Supercomputing e.V. (www.gauss-centre.eu) for funding this project by providing computing time (via grant pn34qu) on the GCS Supercomputer SuperMUC-NG at the Leibniz Supercomputing Centre (www.lrz.de). In addition, the author acknowledges CEDIA (www.cedia.edu.ec) for providing access to their HPC cluster and for the technical support and expertise provided by CEDIA's staff.

Pablo Sebastián Navarrete Piedra

Resumen

El medio interestelar (ISM, por sus siglas en inglés) ha sido objeto de numerosos estudios a lo largo de los años debido a su relevancia en la evolución de las galaxias. Está compuesto por polvo y gas a diferentes densidades y temperaturas, lo que lo hace multifásico y altamente turbulento. Nuestra Galaxia tiene varias regiones de formación estelar, y se cree que algunas de ellas surgen de colisiones entre nubes. Estas colisiones generan ondas de choque que pueden alterar la estructura física y química del gas. Estudiar la formación y evolución de estas ondas es fundamental para comprender la formación de estrellas y la evolución de las galaxias. Desarrollamos y utilizamos un nuevo algoritmo basado en Python para detectar ondas de choque y estudiar las propiedades y distribución del gas en colisiones entre nubes interestelares. Estas interacciones se estudian mediante simulaciones numéricas 3D con diferentes condiciones iniciales, acorde con las leyes de Larson. Identificamos tres etapas en la evolución de las colisiones entre nubes: etapa de compresión, etapa de atravesar la nube y la etapa de disipación. También variamos el tamaño de una de las nubes y las velocidades de colisión. Las nubes más grandes facilitan la erosión de la nube y la formación de ondas de choque más numerosas y potentes en las etapas iniciales, mientras que velocidades de colisión más altas favorecen la aparición de números de Mach más elevados. La distribución de las ondas de choque también varía con el tiempo, ya que los choques fuertes solo se producen en las primeras etapas. A medida que evolucionan las colisiones, la energía cinética turbulenta se disipa rápidamente, por lo que la mayoría de las perturbaciones se convierten en ondas subsónicas en etapas avanzadas. Nuestro estudio sugiere que las ondas de choque con números de Mach inferiores a 10 son intrínsecas a las colisiones interestelares.

Palabras clave: Medio interestelar, Ondas de choque, Ondas subsónicas, Número de Mach.

Abstract

The interstellar medium (ISM) has been extensively studied over the years due to its importance in galaxy evolution. It comprises dust and gas at different densities and temperatures, making it multiphase and highly turbulent. Our Galaxy has several star formation regions, some of which are thought to originate in cloud-cloud collisions. Cloud-cloud collisions produce shock waves that can change the physical and chemical structure of the gas. Studying shocks and how they form and evolve is essential to understanding star formation and galaxy evolution. We present and use our new Python-based shock-finding algorithm to study the gas properties and distribution of shocks in interstellar cloud-cloud collisions. Such interactions are studied via 3D numerical simulations with different initial conditions, consistent with the Larson laws. We identify three stages in the evolution of cloud-cloud collisions, namely, the compression, pass-through, and dissipation stages. We also vary the size of one of the colliding clouds and the collision velocities. Larger clouds facilitate cloud erosion and the formation of more and stronger shocks at early stages, while higher collision velocities promote the emergence of higher shock Mach numbers. Shock distributions are also time-dependent, as strong shocks are only produced during the early stages. As the collisions evolve, turbulent kinetic energy is rapidly dissipated, so the majority of perturbations become subsonic waves at late times. Our study implies that shocks with Mach numbers < 10 are intrinsic to interstellar collisions.

Keywords: Interstellar Medium, Shock waves, Subsonic Waves, Mach number.

Índice general

List of Figures	xviii
List of Tables	xxii
List of Papers	xxiii
1. Introduction	1
1.1. Interstellar medium composition	1
1.2. Gas Phases of Interstellar Medium	3
1.3. Processes in the ISM	4
1.3.1. Turbulence	5
1.3.2. Star Formation	5
1.3.3. Cloud-cloud collisions	5
1.4. Problem statement	8
1.5. General and Specific Objectives	10
2. Shock Detection Algorithm	11
2.1. Shock Theory	11
2.1.1. Velocity gradient across the shock	14
2.2. Python Shock-Finding Routine	15
2.2.1. Mach Number Calculation	17
3. Methodology	19
3.1. Simulation of cloud-cloud collisions	19
3.1.1. Computational Requirements	19
3.1.2. Software	20
3.2. Setup of Our Numerical Simulations	20
3.2.1. Polytropic Index, γ	20
3.2.2. Mean Particle Mass, μ	21

3.2.3.	Larson Laws	21
3.2.4.	PLUTO set-up	22
3.2.5.	Initial and Boundary Conditions	23
3.2.6.	Diagnostics	25
3.3.	Data Analysis	25
3.3.1.	Shock detection algorithm	26
4.	Results & Discussion	29
4.1.	Evolution of interstellar cloud-cloud collisions	29
4.2.	On the effect of cloud size	35
4.3.	On the effect of varying the collision velocity	38
4.4.	Evolution of shock the shock distribution	42
4.4.1.	Time evolution of shock Mach numbers	45
5.	Conclusions & Outlook	49
A.		53
	Bibliography	55

Índice de figuras

1.1.	Left panel shows an artist impression of the Milky Way galaxy pinpointing some of the main spiral arms and the Sun location. The white, blue, and red represent stars. The dust is visible as darker spots. Credit: NASA/JPL-Caltech/R. Hurt (SSC/Caltech). On the right panel, we show an image of the so-called Pillars of Creation, which is a star-forming region where we can see the dust that is hiding the young stars forming inside the pillars. We can also see that the pillars are evaporating due to the radiation of nearby young stars towards the top-right side of the image. The Eagle Nebula is located in the Sagittarius arm. Credits: NASA, ESA, CSA, STScI; Joseph DePasquale (STScI), Anton M. Koekemoer (STScI), Alyssa Pagan (STScI).	2
1.2.	Left panel presents the initial condition where the left cloud is moving towards the larger cloud to its right with a set velocity. The compression of the big cloud can be noticed in the middle panel and the formation of the U shape. The right panel also shows the final stages where the two clouds have merged, but the U shape remains. The plots represent slices of the density [g cm^{-3}] at $Z = 0$. Images obtained for training simulation.	6
1.3.	The left panel shows the evidence of the collision of two clouds observed on the transition of $^{12}\text{CO}(J3 - 2)$. Where the O star represents a white cross, the circles filled in white and black represent the young stars of class I/0 and class II. The contours in red and blue represent each of the clouds moving with mean velocities of 2 km s^{-1} and $8,5 \text{ km s}^{-1}$, respectively, while the green contour shows the bridge, which is labeled as BR1, BR2, and BR3. The right panel represents the declination–velocity diagram of the $^{12}\text{CO}(J3 - 2)$ emission integrated over the range between the black lines of the left panel, and also it shows the velocity bridge marked with the rectangle in the middle of the image. Image taken from Fukui <i>et al.</i> (2021).	9
2.1.	The black line represents the shock front separating two regions: the pre-shock (in red) and the post-shock (in blue). Each of them has different values of ρ , T, p	12
2.2.	Jump in density (r) map, the X-axis shows the Mach number while the Y-axis shows the polytropic index. The three lines remark how the factor r changes fixing γ for mono-atomic, di-atomic, and quasi-isothermal gas changing the Mach number. The labels for the values of γ are shown in the right upper corner.	14

2.3.	Jump in density r for fixed valued of γ for mono-atomic, di-atomic, and quasi-isothermal gas. There is a scaling effect in the maximum value that the jump in density has as we reach $\gamma = 1$. The jump in density r gets higher values.	15
2.4.	Jump in pressure (R) map, the X-axis shows the Mach number while the Y-axis shows the polytropic index. The three lines remark how the factor $R = \frac{p_2}{p_1}$ changes fixing γ for mono-atomic, di-atomic, and quasi-isothermal gas and changing the Mach number. The labels for the values of γ are shown in the right upper corner. The color bar shows the values of R	16
2.5.	Jump in pressure for γ fixed for mono-atomic gas, di-atomic gas, and quasi-isothermal. Mono-atomic gas and di-atomic gas present the same behavior, while the quasi-isothermal presents a less jump on pressure.	17
3.1.	Third Larson's law: relates the number density compared as a function of the cloud size (diameter). The blue line represents the values that Larson's law may take for different masses. The green and yellow diamonds show the initial condition for the Habe Ohta model and the identical cloud model, respectively.	22
3.2.	Larson's law: obtained from the first and the second Larson's law, which relates the cloud size (diameter) with the cloud mass. the blue line represents the values that Larson's law may take for different masses. The green and yellow diamonds show the initial condition for the Habe Ohta model and the identical cloud model, respectively	23
3.3.	Maps of 2D slices at $X=2.5$ [pc], $Y=0$ pc and $Z=0$ pc of density at time $t = 0$ in the standard model ($m24_v030$ s). The small denser cloud is the cloud that is moving, and the larger cloud is the initially non-moving cloud. The color bar is in logarithmic scale	25
3.4.	Flowchart of how our shock-finding algorithm works. The input files are VTK files, and the output files are images showing the shock Mach numbers.	27
4.1.	Density maps of different panels at different times in cloud collision. The left panels show slices at $X = 2.5$, the middle panels at $Y = 0$, and the right panels slice at $Z = 0$. The color bar is in a logarithmic scale.	30
4.2.	Temperature maps of different panels at different times in cloud collision. The left panels show slices at $X = 2.5$, the middle panels at $Y = 0$, and the right panels slice at $Z = 0$. The color bar is in a logarithmic scale.	31
4.3.	Pressure maps of different panels at different times in cloud collision. The left panels show slices at $X = 2.5$, the middle panels at $Y = 0$, and the right panels slice at $Z = 0$. The color bar is in a logarithmic scale.	32

4.4. Diagnostics curves of the evolution of the colliding clouds. Panel A shows the average number density n . Panel B displays the average thermal pressure. Panel C shows the average sound speed, while panel D shows the average temperature. At the bottom panels, we can find the average velocity dispersion (panel E) and median Mach number (panel F). The moving cloud is shown in red, while the initially non-moving cloud is shown in blue. The black lines mark the times that are represented in Figures 4.1-4.3.	34
4.5. Density maps on different planes. The color bar is on a logarithmic scale. Top row Standard model where clouds of different sizes, bottom row identical cloud model two clouds of the same size are colliding	36
4.6. Diagnostics curves of the moving cloud at the evolution of cloud collision varying the size of the moving cloud. The number density n is shown in panel A, the pressure on panel B, on the middle panels on left sound speed (panel C), while panel D shows temperature, the velocity dispersion (panel E), and median Mach number (panel F). Labels are presented in panel B, where the standard model is present in solid line, and clouds of diameters of 2 pc and 4 pc are shown in red and blue, respectively.	37
4.7. Density maps for different slices. The color bar is on a logarithmic scale. The top row is the standard model with a collision velocity of 30 km s^{-1} , while the other models have velocities of 20, 50, 70, 90 km s^{-1} from the second row to the bottom row.	39
4.8. Diagnostic curves of the moving cloud for different collision velocities. Labels are presented on the corner of each panel, where the standard model is present in a solid line, with a collision velocity of 30 km s^{-1} while models with a collision velocity of 20, 50, 70, 90 km s^{-1} are presented in color decreasing color gradient in dashed lines. Panel B shows the labels for each velocity.	40
4.9. Diagnostic curves of the initially non-moving cloud for different collision velocities. Labels are presented on the top right panel, where the standard model is present in solid blue lines, with a collision velocity of 30 km s^{-1} while models with a collision velocity of 20, 50, 70, 90 km s^{-1} are presented in color decreasing color gradient in dashed lines. Panel B shows the labels for each velocity.	41
4.10. Maps of 2D slices at $X=0$, $Y=0$ and $Z=0$ of velocity divergence in the standard model ($m24_v030$ see table 3.2.5). Discontinuity zones are depicted in these maps.	43
4.11. Maps of 2D slices at $X = 2.5$, $Y = 0$ and $Z = 0$ of pressure gradient in the standard model ($m24_v030$ see table 3.2.5). Discontinuity zones are depicted in these maps.	44
4.12. Maps of 2D slices at $X = 2.5$, $Y = 0$, and $Z = 0$ of the shock Mach numbers in the standard model ($m24_v030$ see table 3.2.5). Shocks are shown in brighter colors.	46
4.13. Histograms showing the Mach numbers of all of the subsonic and supersonic perturbations (left) and only of supersonic shocks (right) in our standard CCc (model $m24_v030$).	47
4.14. Histograms showing the Mach numbers for the moving cloud of all of the subsonic and supersonic perturbations (left) and only of supersonic shocks (right) in our standard CCc (model $m24_v030$).	47
4.15. Histograms showing the Mach numbers for the initially non-moving cloud of all of the subsonic and supersonic perturbations (left) and only of supersonic shocks (right) in our standard CCc (model $m24_v030$).	48

Índice de cuadros

1.1. Summary of the ISM gas phases	4
1.2. CO isotopologues and transitions for tracing molecular clouds. Information was taken from Armijos-Abendaño <i>et al.</i> , and Zeng <i>et al.</i>	7
1.3. Molecules for trace shocks	7
3.1. Initial conditions in our simulation set. Cloud 1 represents the moving cloud, while Cloud 2 shows values for the initially non-moving cloud.	24
3.2. Initial condition of the different variables analyzed. Cloud 1 represents the moving cloud, while Cloud 2 shows values for the initially non-moving cloud.	26

Capítulo 1

Introduction

Galaxies comprise stars, interstellar dust, interstellar gas, and an unknown matter known as dark matter. All components between stars are known as **interstellar medium (ISM)**, which has been extensively studied in astrophysics due to its importance in galaxy evolution.^{4,5} The abundance of molecular gas in the ISM is strongly correlated with galaxy evolution because it is responsible for star formation.⁶ Young galaxies are expected to have more ISM gas and, therefore, more star formation regions than old galaxies. This characteristic can be observed in the classification of galaxies that show more star formation in young spiral galaxies compared with old elliptical galaxies, which do not have gas.⁷

The abundance of ISM in galaxies has an essential role in the evolution of stars because, on the one hand, the ISM provides the fuel necessary for star formation. On the other hand, at the end of stellar life, supernova explosions enrich the ISM by adding some heavier elements, the so-called "metals" (which are elements different than H and He), for the next generation of stars. Furthermore, stars contribute to the dynamics of the ISM by heating the surrounding material and creating shock waves.^{8,9,5} Figure 1.1 (left panel) shows artist impression of the Milky Way galaxy where it is possible to note the stellar disk, the galactic center, and interstellar dust. Also, the right panel shows an example of Milky Way's star formation region, which illustrates the dynamics of the ISM because it shows that the pillars are evaporating due to the radiation of nearby young stars towards the top-right side of the image.

1.1. Interstellar medium composition

The ISM comprises several components that contribute differently to its dynamics. The ISM components are interstellar gas, dust, cosmic rays, electromagnetic radiation, interstellar magnetic field, gravitational field, and dark matter particles. Their abundance and distribution are not equal, but they all play an essential role in the evolution of the ISM. The main features are described below. For a more detailed explanation, see Gnedin *et al.* (2016).

- **Interstellar gas:** Interstellar gas is the most abundant component of the ISM, representing more than 90 % of the composition. Different species are detected in the gas phase. H and He are the elements with a higher

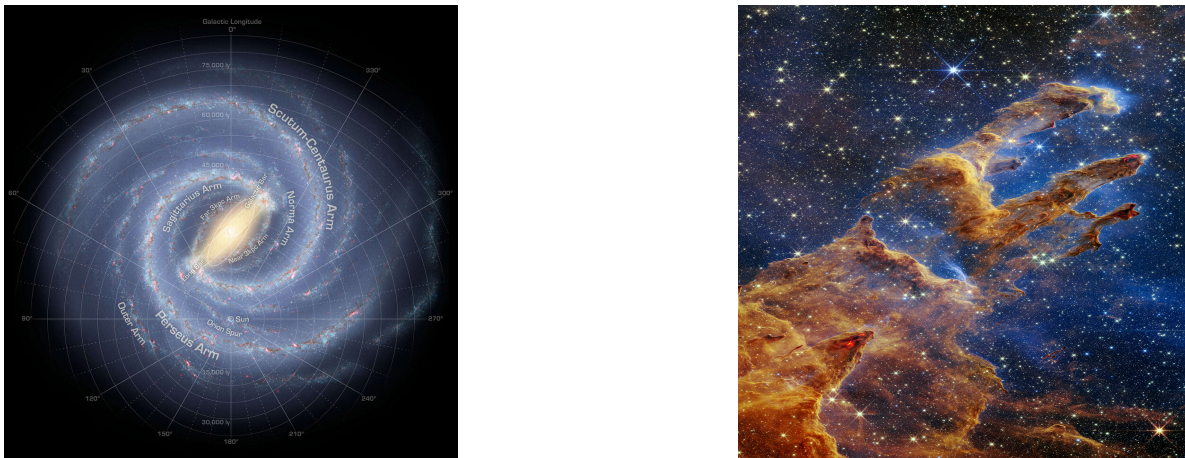


Figure 1.1: Left panel shows an artist impression of the Milky Way galaxy pinpointing some of the main spiral arms and the Sun location. The white, blue, and red represent stars. The dust is visible as darker spots. Credit: NASA/JPL-Caltech/R. Hurt (SSC/Caltech). On the right panel, we show an image of the so-called Pillars of Creation, which is a star-forming region where we can see the dust that is hiding the young stars forming inside the pillars. We can also see that the pillars are evaporating due to the radiation of nearby young stars towards the top-right side of the image. The Eagle Nebula is located in the Sagittarius arm. Credits: NASA, ESA, CSA, STScI; Joseph DePasquale (STScI), Anton M. Koekemoer (STScI), Alyssa Pagan (STScI).

presence accounting for 99% of the ISM gas phase, while the rest are heavier elements. H and He play an important role in star formation because stars are constituted mostly of these two elements.

- **Dust:** The dust in the ISM is composed of tiny solid particles (complex molecular compounds) with irregular shapes and sizes of a few μm . These dust particles come from the early stars and newer stars. Also, it is possible to form dust grains in the ISM as well. Silicates, carbon, iron, and magnesium are elements found together with different ices. Dust will produce **reddening** and **extinction** for star light observation.¹¹ Also, they act as catalytic elements for the formation of new stars due to their help in the formation of the most important molecule (molecular hydrogen H_2 in the ISM clouds. The process is very simple as H atoms remain in the grain surface until they encounter another H and form H_2 .^{12 13}
- **Cosmic rays:** They contribute to the dynamics of the ISM at different energies because they have the potential to alter the interstellar gas morphology, gas phase, and kinematics.^{14 15} Cosmic rays can produce the ionization of some species.¹⁶ Also, cosmic ray pressure and transports can provide support against gravitational instability.^{14 17 15}
- **Electromagnetic radiation (EMR):** The EMR comes from different sources. Most of the EMR comes from interstellar radiation emerging from gas, stars, and the Cosmic Microwave Background (CMB). There are processes associated with the EMR, such as ionization produced by radiation emitted from O and B stars

which can easily ionize the gas near them.¹⁸ Also, cosmic rays are responsible of synchrotron radiation¹⁹, bremsstrahlung radiation from relativistic electrons²⁰.

- **Magnetic Field:** The magnetic field is an important component of the ISM since it can regulate the dynamics and high energy processes occurring in the ISM gas. Magnetic fields provide some stability to ISM clouds against gravitational collapse. Magnetic fields are also part of ISM turbulence because they are involved in dynamos and particle acceleration.^{21 22}
- **Gravitational Field:** gravity is also a crucial ingredient in the star formation process because if an ISM cloud reaches a certain amount of mass (known as Jeans's limit), it would suffer gravitational instability and eventually collapse into a star.²³
- **Dark matter:** Dark matter has not been directly detected yet. However, It directly influences the evolution of galaxies and the ISM because it affects the distribution and motion of stars and gas^{24 25}.

1.2. Gas Phases of Interstellar Medium

ISM clouds are a mixture of the different gas phases, which clouds may be distinguished from one to another by their internal properties, such as velocity, temperature, density, or chemical composition. The ISM is a multiphase medium, which comprises 3 phases and several subcomponents (see Table 1.2). The main phases are the ionized phase, atomic phase, and molecular phase.

- **Ionized Gas:** The ionized gas comprises different ionized species. Each presents distinct characteristics controlled by its physical properties, such as density, temperature, and ionization process. Ionized components can be classified as hot ionized medium (**HIM**), which presents high temperatures ($10^5 - 10^7$ K) and low densities ($10^{-4} - 10^{-2} \text{cm}^{-3}$). H_{II} regions, which is characterized for being a region of star formation, intercloud or diffuse H_{II} , which is a region existing between cloud in the ISM. The warm ionized medium (**WIM**) represents approximately ≈ 90 of the ionized gas. Its ionization is moderate and can be found in the spiral arms of galaxies.^{26 27 10}
- **Atomic Gas:** It is composed of two phases differing from one to another by the temperature. The warm neutral medium **WNM** presents densities of $0,2 - 0,3 \text{g cm}^{-3}$ and temperatures varying from 6×10^3 K to 10^4 K. It constitutes at least the 40 % of the disk of spiral galaxies, and the neutral hydrogen, HI is detected at 21 cm of emission. The cold neutral medium **CNM** is detected in absorption lines, and it is denser than the WNM. It has $20 - 50 \text{g cm}^{-3}$ densities and temperatures $100 - 1000$ K.^{27 10}
- **Molecular Gas:** This is the ISM's most crucial phase because star formation occurs within molecular gas. This has two forms: the dense molecular cloud and the diffuse molecular cloud. Molecular gas is subjected to photoionization radiation from different sources. As was mentioned above, dust plays a key role in forming H_2 because it acts as a catalytic element where some of HI can be attached to the dust particle and stays there until another HI reaches it and react to form H_2 ¹³. Also, H_2 photodissociation can occur.^{27 10}

Cuadro 1.1: Summary of the ISM gas phases

ISM Phase	Composition	Temperature K	Density cm^{-3}
Ionized gas	<ul style="list-style-type: none"> ▪ Warm Ionized Medium (WIM) 	800	0,20 – 0,50
	<ul style="list-style-type: none"> ▪ H_{II} Region 	10^4	$10^2 - 10^4$
	<ul style="list-style-type: none"> ▪ Hot Ionized Medium (HIM) 	$10^5 - 10^7$	$10^{-4} - 10^{-2}$
Atomic gas	<ul style="list-style-type: none"> ▪ Warm Neutral Medium (WNM) 	$6 \times 10^3 - 10^4$	0,20 – 0,30
	<ul style="list-style-type: none"> ▪ Cold Neutral Medium (CNM) 	50 – 100	20 – 50
Molecular gas	<ul style="list-style-type: none"> ▪ Dense H_2 	10 – 20	$10^2 - 10^6$
	<ul style="list-style-type: none"> ▪ Diffuse H_2 	50	~ 10

1.3. Processes in the ISM

The ISM's dynamic nature is controlled by various processes like ionization, radiation, star formation, turbulence, cloud collision, chemical reaction, and other interactions between the different gas phases of the ISM. We explain the most relevant for our work: turbulence, star formation, and cloud collision. It is essential to mention the last one is the main topic of this work.

1.3.1. Turbulence

The ISM is not laminar, and there is evidence that it is turbulent^{28,29}. ISM turbulence has a significant impact on its dynamics due to its influence on the motion of the gas and star formation. ISM turbulence has been probed by studying the distribution of the gas velocity dispersion³⁰ and analyzing the density distribution via different line emissions³⁰ like HCN, CS, HCN.^{31 32 33 34} We can find different types of turbulence in the ISM based on the Mach number M which is the ratio between fluid velocity and the velocity of the sound speed of the fluid: supersonic ($M > 1$), transonic ($M \approx 1$), and subsonic ($M < 1$).²⁹

1.3.2. Star Formation

The ISM has a huge influence on the Star formation because its occurrence is determined by the presence of molecular clouds. The rate at which star formation occurs within galaxies also gives us some estimates on the age of a galaxy because there is typically no star formation in old elliptical galaxies, while young spiral galaxies have a high rate of star formation. However, the star formation rate depends on the galaxies getting extra gas from the companion galaxies. Star formation consumes the gas in the ISM, so with time, there is less available gas to fuel it.

Gravity is what ultimately leads to star formation because when gas pressure is insufficient to stand against gravity and keep hydrostatic equilibrium, then self-gravitational collapse of the molecular cloud occurs. The collapse of molecular clouds creates a protostar which will start accreting gas from its surroundings.³⁵

Physically due to hydrostatic equilibrium, there is a limit for the cloud mass and cloud radius to self-gravitational collapse occurs and are so-called **Jeans mass** and **Jeans length**, respectively.

1.3.3. Cloud-cloud collisions

This is the most relevant process for the present work as we aim to study cloud-cloud collisions (CCc). Gas clouds in the ISM are dynamic structures and can interact between them, creating regions known as cloud-cloud collisions. The CCc can perturb the ISM and trigger star formation because even if the cloud does not satisfy the Jean mass before the collision. The compression from the collision could push the cloud into the critical region for collapse.^{1 36}

Previous simulation of cloud-cloud collisions

Many numerical simulations of CCc have been carried out, each changing some initial condition or parameter according to the computational power available. The first CCc simulation was made by Stone (1970), and consisted of a one-dimensional CCc with this initial condition: two HI clouds with the same size (diameter), densities of $5 - 10 \text{ g cm}^{-3}$, and colliding velocity of 10 km s^{-1} . The author concluded that both clouds are fully destroyed at this collision velocity.³⁷ Observational studies then showed that numerical simulations need to consider molecular clouds (i.e., gas with higher densities). The evolution of computational power also allowed the consideration of new variables in one dimension, such as molecular formation and dissociation or cooling process as radiative gas, and more recently, expanding the models to two-dimensional and three-dimensional setups. Some three-dimensional models were made

considering smooth particle hydrodynamics (**SPH**). Many variations of this were made by changing the cloud's size, changing the number of particles of the SPH algorithm, adding turbulence to the medium, considering UV feedback from the former star, and adding self-gravity.¹ Previously, it was mentioned that the magnetic field is a component of the ISM, and magneto-hydrodynamics simulations have been carried out for the CCc.

Based on all these studies, it is possible to classify the CCc into two types considering the difference in the size of both clouds: an idealized model where two clouds of the same size collide and a more general model where a small cloud collides with a cloud of larger size. The first case is difficult to find in the ISM. However, it can still provide some valuable insights into the physics of the colliding gas clouds. The second is known as the “*Habe–Ohta model*”, which may include self-gravity and magnetic fields³⁸. Simulations have provided some characteristic features of the evolution of CCc, which is normally split into three different stages. Initial stage (**Stage I**): the two clouds approaching each other in a collisional trajectory. Intermediate stage (**Stage II**): gas layers start to compress, and **U shape** appears as the small cloud enters the large. The final stage (**stage III**): The gas cloud of the small cloud merged with the gas of the larger cloud, but U shape has not disappeared.¹ All of these phases can be seen in figure 1.2. Three main features characterize the CCc according to simulation and are also found in observational studies. These are the following: a) *Complementary density distribution with displacement*, b) *bridge on velocity*, c) *U shape*. For more details, see a review by Fukui *et al.*¹.

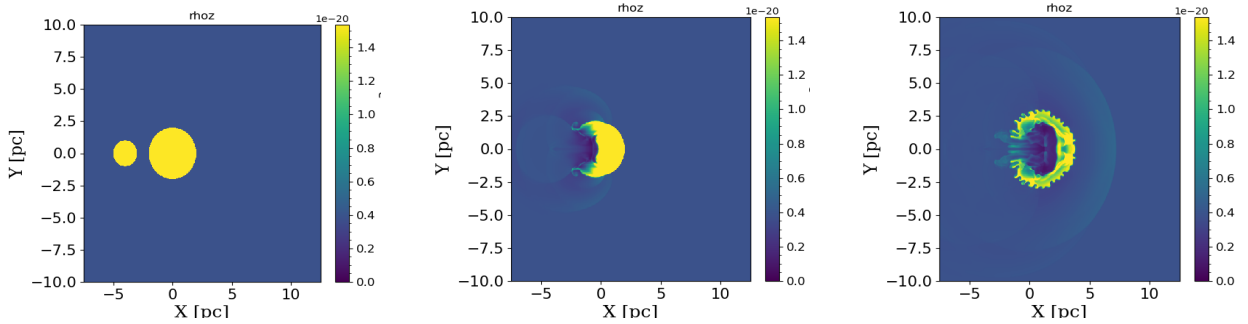


Figure 1.2: Left panel presents the initial condition where the left cloud is moving towards the larger cloud to its right with a set velocity. The compression of the big cloud can be noticed in the middle panel and the formation of the U shape. The right panel also shows the final stages where the two clouds have merged, but the U shape remains. The plots represent slices of the density [g cm^{-3}] at $Z = 0$. Images obtained for training simulation.

Observational Evidence of cloud-cloud Collisions

Observational evidence corroborates the numerical simulation about the triggers of star formation by the CCc.^{39 40 41 42} Detecting molecular hydrogen H_2 in astronomical observations represents a challenge and requires the use of different tracers. There are many molecules in the ISM. In fact, more than 200 molecular species have been detected. All of them can be used to trace the density of molecular gas. The most used tracer for the density

of molecular gas is CO and its isotopologues in their different transitions. However, most studies rely on the CO (J (1-0)) transition because of its strong emission signal.^{43 44} The detection of CO is possible using radio telescopes such as the Atacama Large Millimeter/submillimeter Array (ALMA), Institut de Radioastronomie Millimétrique (IRAM 30m), and others.^{45 46} There is a relation between the integrated intensity of transitions of the CO and the column density($N(H_2)$), which is expressed as a conversion factor denoted as X_{CO} .⁴⁷ This value will vary in different environments depending on the physical properties.

$$N(H_2) = X_{CO} \times W(CO) \quad (1.1)$$

where

$$W(CO) = \int T(v)dv \quad (1.2)$$

The value of the X_{CO} more used is $4 \times 10^{20} (\text{cm}^{-2} (\text{K km})^{-1} \text{s}^{-1})$. Table 1.2 presents the CO isotopologues and their transitions.

Cuadro 1.2: CO isotopologues and transitions for tracing molecular clouds. Information was taken from Armijos-Abendaño *et al.*, and Zeng *et al.*.

CO isotopologues	Transition	Frequency GHz
^{12}CO	J (1-0)	115.00
^{13}CO	J (1-0)	110.20
^{18}CO	J (1-0)	109.80

In addition to density tracers, there are also molecular species that are produced by the shocks, so they are natural shock tracers such SiO , HNCO , CH_3OH , and others. The importance of shocks for the ISM dynamics is because they emerge in several processes, such as cloud-cloud collisions and interstellar winds, and are responsible for heating up the gas they pass through. Shock tracing is then done using species that need specific conditions that are only provided by shocks. The most commonly used shock tracers are presented in Table 1.3

Cuadro 1.3: Molecules for trace shocks

Molecules	Transition	Frequency GHz
SiO	J (2-1)	86.80
HNCO	J (10-9)	219.79
CH_3OH	J (4-3)	218.44

Most of the candidate ISM regions to host CCc are zones of high-rate star formation. Fukui *et al.* (2018), in his work, lists several high-mass star-forming regions that CCc could have triggered⁴⁸. Below we summarize the observations of 4 ISM regions: SgrB2, RCW 120, M43, and M20. Each of these regions presents some of the characteristic features of cloud-cloud collisions.

- **Sagittarius B2:** Sagittarius B2 cloud is a giant molecular cloud with a high abundance of the known molecular species. It is at a distance 100 pc from the galactic center (Sagittarius A*). It is important because its star-forming rate (SFR) is slightly higher than the star-formation rate of the molecular cloud in the Milky Way's disk. It contains 3 different protoclusters named Sagittarius N (north), Sagittarius M (middle), and Sagittarius S (south).² This region contains compact and ultra compact H_{II} region and high-mass young stellar objects (YSO).⁴⁹ The distribution of gas at different velocities and the existence of molecules such as *SiO*, *HNCO*, *CH₃OH* suggest a cloud-cloud collision as the trigger of star formation in this region. Sato *et al.* (2000) studied the ¹³CO(1-0). They found that the distribution of velocity in emission maps shows the formation of a hole, with edges that spatially correlate with a clump at different velocities which can be interpreted as a result of a cloud-cloud collision. Another evidence of cloud collision is studying the shock tracer as was made by Armijos-Abendaño *et al.* (2020), and Zeng *et al.* (2020). Observations and numerical studies of SiO (J=2-1) maps were reported². Their results show that a cloud-cloud collision can explain the dynamics and structures of this region by analyzing this shock-tracing molecule.
- **RCW 120:** This is a round H_{II} region, which is created by a high-mass O star. It is located around 1.3 pc from the Sun. It is a region of interest because it presents YSO along the ring of the H_{II} region, which indicates that star formation may have been triggered by the intense ionizing radiation of the star inside the H_{II} region. In this region, two clouds were detected by studying two transitions, namely: CO(J = 1-0) and (J = 3-2)³⁹. Torii *et al.* (2015). postulate that a cloud-cloud collision will trigger star formation in this region, producing a cavity (U shape on the Habe-Ohta model) where the star is located.
- **M42:** M42 is the nearest young high-mass star-forming region around 412 pc from the Sun. Also, it is known as the Orion Nebula Cluster(ONC) with its companion M43. The result presented by Fukui *et al.*(2018) show clouds at two different velocity components and also found a possible region where the distribution of gas velocities complement each other in accordance with numerical simulations.
- **M20:** The Trifid Nebula M20 is a H_{II} region that is ionized by an O star. Torii *et al.*(2017) studied ¹²CO (J =1-0) and (J=3-2) emission from two colliding clouds. They found that clouds present a spatial complementary distribution that presents 3 different bridges connecting the two cloud velocities (see Figure 1.3).

1.4. Problem statement

There is substantial evidence, both observational and numerical which suggests that cloud-cloud collisions can trigger star formation. Certain regions of our Galaxy, such as Sagittarius B2, M20, and RC120, among others, exhibit star formation as a result of shocks produced by CCc. Similarly, Over time, numerous numerical simulations have been conducted to investigate the characteristics of CCc. One of the most used models is the Habe-Ohta model. However, there are gaps in our understanding, especially concerning the impact of varying initial conditions. Factors such as collision velocity, cloud size, the subsequent compression of gas, distribution of shocks, and Mach numbers have either been unexplored or remain not well understood. This thesis seeks to explore these gaps. Specifically,

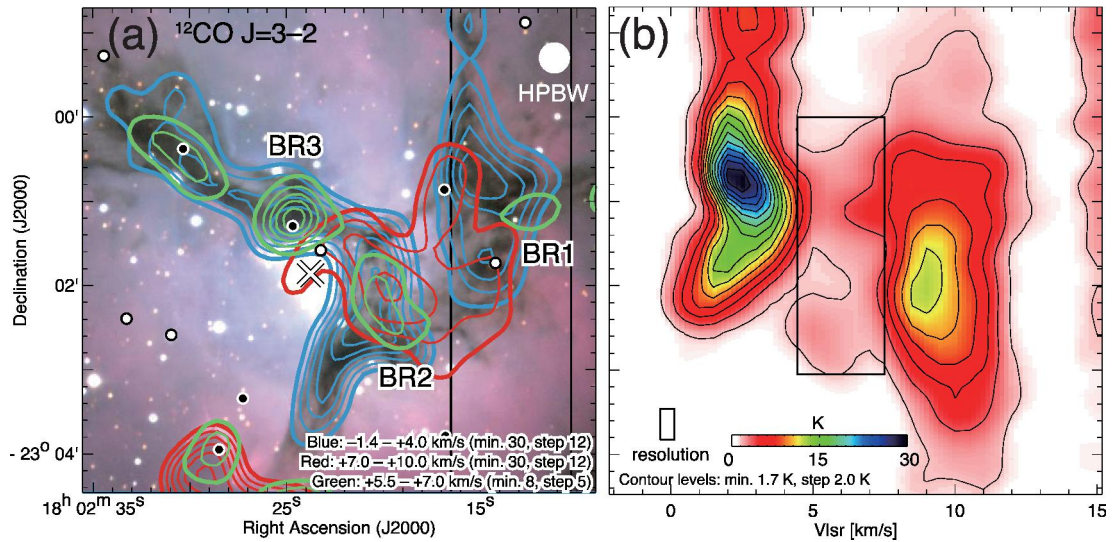


Figura 1.3: The left panel shows the evidence of the collision of two clouds observed on the transition of $^{12}\text{CO} (J=3-2)$. Where the O star represents a white cross, the circles filled in white and black represent the young stars of class I/0 and class II. The contours in red and blue represent each of the clouds moving with mean velocities of 2 km s^{-1} and 8.5 km s^{-1} , respectively, while the green contour shows the bridge, which is labeled as BR1, BR2, and BR3. The right panel represents the declination-velocity diagram of the $^{12}\text{CO} (J=3-2)$ emission integrated over the range between the black lines of the left panel, and also it shows the velocity bridge marked with the rectangle in the middle of the image. Image taken from Fukui *et al.* (2021).

we will investigate how alterations in cloud size and collision velocities influence the physical outcomes when two clouds collide. By understanding these variations, we aim to provide a more comprehensive insight into the processes governing the gas dynamics of colliding clouds.

1.5. General and Specific Objectives

This thesis aims to understand how changes in the initial conditions of simulations of cloud-cloud collisions, such as the diameter of the clouds and the collision velocity, affect the physical properties of the gas. For this, we use three-dimensional, quasi-isothermal, hydrodynamical simulations. Additionally, we aim to find perturbations in such gas and classify them into shock waves (Mach number, $M > 1$) and subsonic waves (Mach number $M < 1$). To achieve this, we study the perturbation distribution as a function of the initial conditions through shock-finding algorithms developed using the hydrodynamical Rankine-Hugoniot jump conditions (see Chapter 2). The specific research objectives are the following:

- Perform hydrodynamical simulations to analyze the evolution of interstellar cloud-cloud collisions.
- Develop a Python-based shock-finding algorithm based on the hydrodynamical Rankine-Hugoniot jump conditions.
- Detect shock waves and characterize them using our shock-finding algorithm and Python code.
- Compare the implications of changing initial conditions on the gas evolution and the generation of shock waves.

This work is structured as follows. Chapter 2 presents a summary of the theory of shocks and how the hydrodynamical approach will describe them. Additionally, this chapter outlines the algorithm to detect shock waves. Chapter 3 presents the methodology, computational tools, and algorithms used to simulate cloud-cloud collisions using hydrodynamical models. Also, it presents the initial conditions and a short description of how we set up the simulations. Chapter 4 shows the results of our simulation and presents the comparisons of different initial conditions. Finally, Chapter 5 summarizes the findings of this thesis.

Capítulo 2

Shock Detection Algorithm

In this chapter, we introduce the concepts and formalism of the hydrodynamic shock theory and describe an algorithm to detect shocks in numerical simulations of this process.

2.1. Shock Theory

Waves are perturbations that propagate in fluids, such as gases. Waves can be classified according to their velocity (v) relative to the sound speed of the medium (c):

- Subsonic waves when: $v < c_s$
- Transonic waves when: $v = c_s$
- Supersonic waves when: $v > c_s$

Wave propagation is smooth if the wave travels subsonically at $v < c_s$. However, if $v > c_s$, the wave turns into a shock wave. The main characteristic of shock waves is that they separate two regions of the fluid with different local properties (temperature T , density ρ , pressure p), as we can see in figure 2.1 with the unperturbed region referred to as the pre-shock region, and the disturbed region referred to as the post-shock region. Notice that each region's location depends in the shock's propagation direction. In this context, if the shock propagates to the right in figure 2.1, the pre-shock is the region on red while the post-shock is in blue.

The gas dynamic equations describe how waves propagate through a medium. There are two approaches to solving these problems: Magneto-hydrodynamics (MHD) and Hydrodynamics (HD). As the name suggests, magnetic fields are considered in the first case, while they are neglected in HD. In this work, we do not include magnetic fields, so much MHD shocks are not studied.

The set of equations (2.1-2.3) are used to describe the different kinds of HD- shocks that exist. There are parallel shocks, perpendicular shocks, and oblique shocks, each with their main characteristics. We use the HD equations to

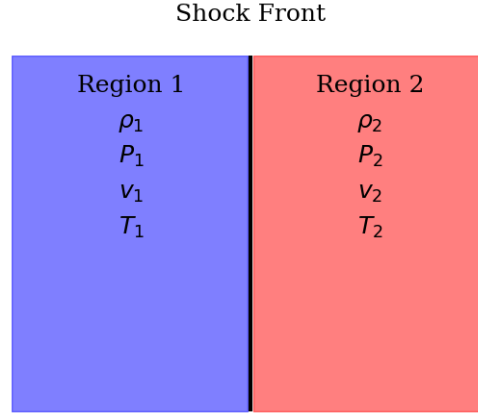


Figura 2.1: The black line represents the shock front separating two regions: the pre-shock (in red and the post-shock (in blue). Each of them has different values of ρ , T , p

derive the so-called HD Rankine-Hugoniot conditions. The HD expressions read.

$$\left[\frac{\partial \rho}{\partial t} + \nabla \cdot (\rho \vec{v}) \right] = 0 \quad (2.1)$$

$$\left[\frac{\partial \rho \vec{v}}{\partial t} + \nabla \cdot T \right] = 0 \quad (2.2)$$

$$\left[\frac{\partial U}{\partial t} + \nabla \cdot \vec{u} \right] = 0 \quad (2.3)$$

Where T is the total stress tensor, \vec{u} , energy flux density, and U , the total energy density, each of them is defined as represented below.

$$T = \rho \vec{v} \vec{v} + p I \quad (2.4)$$

$$U = \frac{1}{2} \rho v^2 + \frac{p}{\gamma - 1} \quad (2.5)$$

$$\vec{u} = \left(\rho v^2 + \frac{\gamma}{\gamma - 1} p \right) \vec{v} \quad (2.6)$$

Using equations (2.1-2.3), (2.4-2.5) and the conservation of mass, momentum, and energy on both sites of the shock, we derive the simplified Rankine Hugoniot jump conditions (2.7-2.9), which establish the behavior of the gas

across the shock as a function of the specific heat capacity ratio γ and the Mach number M .

$$\vec{v}_s (\rho_2 - \rho_1) = \rho_2 v_2 - \rho_1 v_1 \quad (2.7)$$

$$\frac{\rho_2}{\rho_1} = \frac{v_1}{v_2} = r = \frac{(\gamma + 1) M_1^2}{(\gamma - 1) M_1^2 + 2} \quad (2.8)$$

$$\frac{p_2}{p_1} = R = \frac{(\gamma + 1) r - (\gamma - 1)}{(\gamma + 1) - (\gamma - 1) r} \quad (2.9)$$

The Mach number, M , represents the ratio of the velocity perturbation to the sound speed of the medium. This describes how fast the perturbation is compared to the sound speed in the medium.

$$M = \frac{v_s}{c} \quad (2.10)$$

From the Rankine-Hugoniot jump conditions, we can study the behavior of pressure p and density ρ on both sites of the shock (pre-shock and post-shock) using color maps where the color represents the ratio between the pressures and densities in each region (see Figure 2.2-2.5). Equations 2.8, and 2.9 represent the jump in density and pressure, respectively. For such calculation, γ changes from 1-2 with steps of 0.1 while the Mach number goes from 1 to 25.

The color map in Figure 2.2 shows the jumps in density at different values of γ and M . Notice that the color change is not evident in all figure regions. Also, there are regions where the values of $\frac{\rho_2}{\rho_1}$ take values more significant than 1, specifically for values of γ around 1.1 to 1.2, where an increase in Mach number produces a more perceptible color change. The more prominent difference in color occurs when M takes values less than five. Below these M , there is a stabilization in the post and pre-shock pressure ratio. On the map, there are three lines, one in red representing the evolution of the jump in density for mono-atomic gas, black representing di-atomic gas, and blue quasi-isothermal gas.

Figure 2.3 shows the change in density for fixed values of $\gamma = \frac{5}{3}$, $\gamma = \frac{7}{5}$, and $\gamma = 1,01$ as they help show more detail the color change as M increases. Analyzing figure 2.3, the evolution of the factor r shows a rapid growth for small values of the Mach number, but then it plateaus for large Mach numbers. Also, as γ approaches ~ 2 , the maximum value for r becomes smaller. The maximum value for a mono-atomic gas is approximately 4, while for a diatomic gas is ~ 6 . Another essential remark is that the convergence to these values starts for $M \approx 5$ in mono-atomic gases and $M \approx 9$ for diatomic gases. There is a great difference in the increases of the jump densities for quasi-isothermal gas because the gas is more compressible owing to the softer value of γ .

After studying the density behavior in shocks, another property used to determine how the gas interacts with its medium is the jump in pressure, R , relating to the pressure in the pre-shock and the post-shock regions.

Figure 2.4 presents maps of the pressure jumps, R , which have some difference from figure 2.2 where the color decreases as γ increases, but for this case, the color intensity increase on Mach axis. Analyzing color representation, we can see the formation of bands in the M axis for small Mach numbers, and variation inside the bands is not noticeable. Observing the variation for $\gamma = \frac{5}{3}$ and $\gamma = \frac{7}{5}$ in figure 2.4, they exhibit approximately the same behavior because of the bands present in the color map. The behavior of the pressure jump for quasi-isothermal takes lower values compared with mono-atomic gas and di-atomic gas.

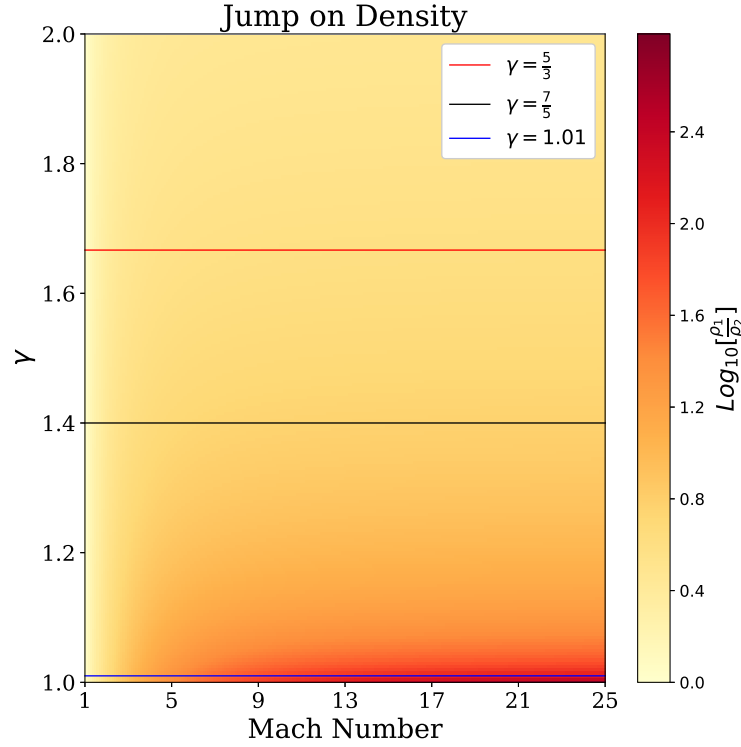


Figura 2.2: Jump in density (r) map, the X-axis shows the Mach number while the Y-axis shows the polytropic index. The three lines remark how the factor r changes fixing γ for mono-atomic, di-atomic, and quasi-isothermal gas changing the Mach number. The labels for the values of γ are shown in the right upper corner.

2.1.1. Velocity gradient across the shock

As we use the shock theory to design our shock-finding routine, we need to find an expression for velocity difference across the shock. The calculation of the shock Mach number in numerical simulations can be derived using mass conservation, equation 2.8, and momentum conservation. To achieve this, v_2 is defined as a function of densities and v_1 .

$$v_2 = \frac{\rho_1 v_1}{\rho_2} \quad (2.11)$$

combining equation 2.11 and 2.8 and obtain the following relation.

$$v_2 = \left(\frac{(\gamma - 1)M_1^2 + 2}{(\gamma + 1)M_1^2} \right) v_1 \quad (2.12)$$

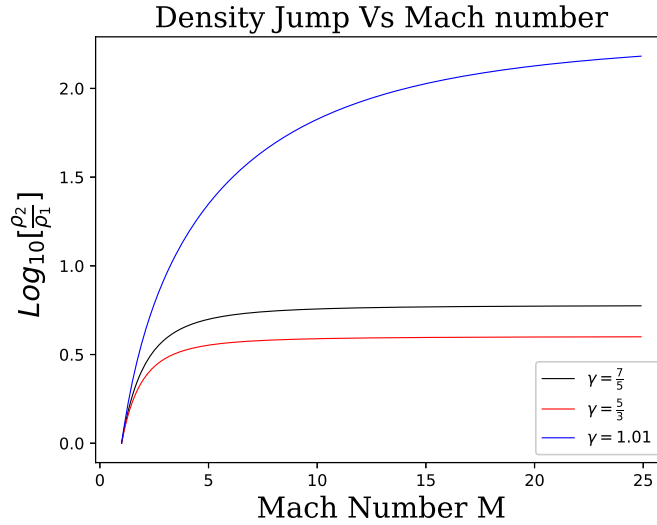


Figura 2.3: Jump in density r for fixed value of γ for mono-atomic, di-atomic, and quasi-isothermal gas. There is a scaling effect in the maximum value that the jump in density has as we reach $\gamma = 1$. The jump in density r gets higher values.

considering v_1 as v_s , the velocity of the shock and getting the velocity difference between the pre-shock and post-shock $\Delta v = v_2 - v_1$. After replacing v_2 with 2.12 obtain the following relation.

$$\Delta v = \left(\frac{(\gamma - 1)M^2 + 2 - (\gamma + 1)M^2}{(\gamma + 1)M^2} \right) v_s \quad (2.13)$$

Equation 2.13 can be simplified even more and expressed as:

$$\Delta v = \left(\frac{\gamma - 1}{\gamma + 1} + \frac{2}{(\gamma + 1)M^2} - 1 \right) v_s \quad (2.14)$$

Notice that the second term inside the parenthesis goes to 0 for $M \gg 1$. We use equation 2.14 to estimate the shock Mach numbers in our algorithm. Using the simplified version of this equation for strong shocks (i.e. without the second term) is also possible, but it would introduce some errors for weak shocks, so we use the full equation in our code.

2.2. Python Shock-Finding Routine

The detection of the shocks and the calculation of their respective Mach number can be done considering velocities, temperature, and entropy jumps according to the methods presented in Vazza *et al.* (2011), Lehmann *et al.* (2016), and Teutloff (2021). Based on the algorithms presented in these studies, we developed our own Python

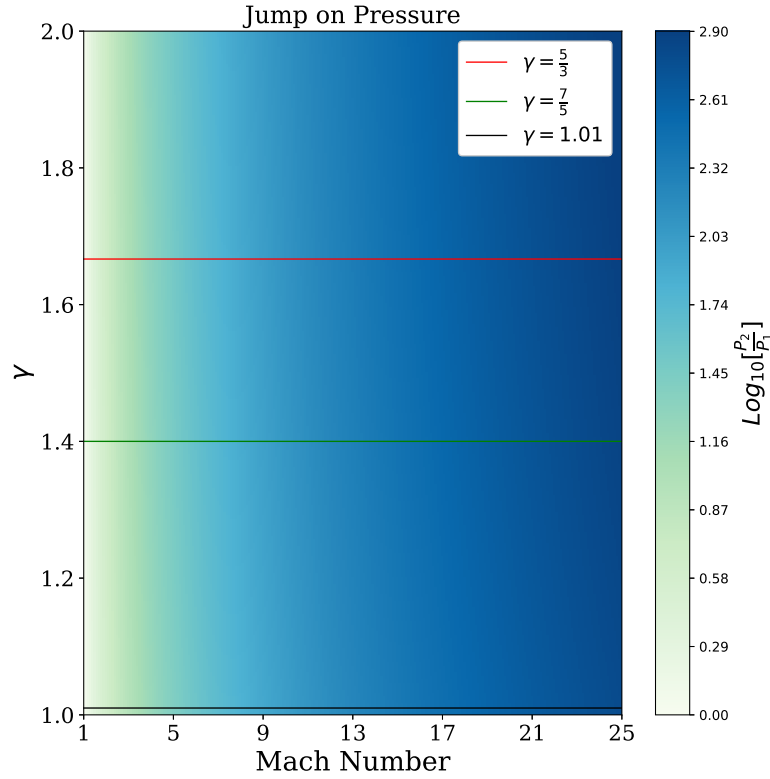


Figura 2.4: Jump in pressure (R) map, the X-axis shows the Mach number while the Y-axis shows the polytropic index. The three lines remark how the factor $R = \frac{p_2}{p_1}$ changes fixing γ for mono-atomic, di-atomic, and quasi-isothermal gas and changing the Mach number. The labels for the values of γ are shown in the right upper corner. The color bar shows the values of R

routine to detect hydrodynamical shocks in numerical simulations of the CCc. Our shock finding algorithm is based on the Rankine-Hugoniot jump conditions, especially on equations 2.8, 2.9, and 2.14. The method used in this thesis is based on the velocity jump (VJ) method by Vazza *et al.* (2011), which considers the pressure gradient and the velocity divergence in the gas as inputs to find shocks. This method searches for significant changes in the pressure of the flow and for convergence flows. The VJ method establishes that candidate cells must satisfy two conditions:

1. $\vec{\nabla} \cdot \vec{v} < 0$
2. $|\vec{\nabla} p| > \Pi$

where Π is a threshold.

The program searches for convergent flows and pressure gradients larger than Π , where the derivatives can be approximated by the central differences method (equation 2.15). We use the *numpy* library to calculate the gradient

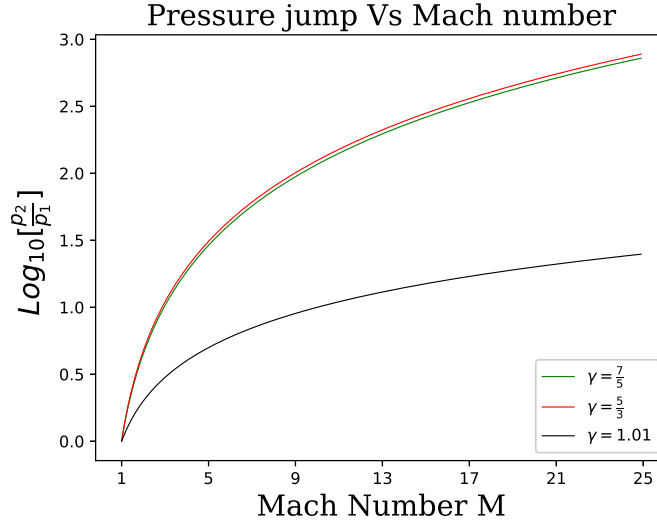


Figura 2.5: Jump in pressure for γ fixed for mono-atomic gas, di-atomic gas, and quasi-isothermal. Mono-atomic gas and di-atomic gas present the same behavior, while the quasi-isothermal presents a less jump on pressure.

and divergence of the input variables using the function `numpy.gradient()`, which uses the equation 2.15 where x is pressure or density and h represents the small variation of the variable.

$$f'(x_i) \approx \frac{f(x_i + h) + 2f(x_i) - f(x_i - h)}{h^2} \quad (2.15)$$

2.2.1. Mach Number Calculation

The Rankine-Hugoniot jump conditions enable the calculation of the Mach numbers M evaluating the thermodynamical state of the pre-shock region (un-perturbed gas) and post-shock region (perturbed gas). The difference in the physical conditions (density, pressure, and temperature) between the pre-shock and post-shock regions are used to determine the Mach number. First, we calculate the sound speed in each of the cells.

$$C_s = \sqrt{\gamma \frac{P}{\rho}} \quad (2.16)$$

where P and ρ are the thermal pressure and density for each cell from the simulations, respectively. Determining the location in the computational domain of the pre-shock and post-shock regions with respect to a cell represents a challenge. To determine this, we move the grid one cell in all directions (X, Y, Z) and find the minimum sound speed, which corresponds to that in the pre-shock region. This ensures the use of the pre-shock sound speed because it is smaller than the post-shock. We need to calculate the Mach number in each cell of the computational domain.

From equation 2.14, the equation for Mach numbers components gets:

$$M_{x,y,z} = \frac{-\nabla v_{x,y,z}(1 + \gamma) + \sqrt{16c_s^2 + \nabla v_{x,y,z}^2(1 + \gamma)^2}}{4c_s} \quad (2.17)$$

where $\nabla v_{x,y,z}$ is the directional speed.

$$\nabla v_x \approx \left| \frac{\partial v_x}{\partial x} \right| (2\Delta x) \quad (2.18)$$

$$\nabla v_y \approx \left| \frac{\partial v_y}{\partial y} \right| (2\Delta y) \quad (2.19)$$

$$\nabla v_z \approx \left| \frac{\partial v_z}{\partial z} \right| (2\Delta z) \quad (2.20)$$

Once $M_{x,y,z}$ is obtained, the total Mach number needs to be calculated in each cell as

$$M = \sqrt{M_x^2 + M_y^2 + M_z^2} \quad (2.21)$$

The waves with a $M > 1$ are shock waves, the ones with $M = 1$ are transonic waves, while subsonic waves have Mach numbers $M < 1$.

For determining the turbulence, we can calculate the M_{rms} (equation 2.22), which is the ratio between the velocity dispersion σ_v and the sound speed.

$$M_{rms} = \frac{\sigma_v}{C_s} \quad (2.22)$$

Capítulo 3

Methodology

To study shocked gas structure in interstellar cloud-cloud collision, we resort to numerical simulations where two different clouds interact under different initial conditions to produce a set of data outputs that we can analyze post-processing. All the elements used in this work are described below.

3.1. Simulation of cloud-cloud collisions

The tools employed will be classified into 1) the software needed to develop the simulation, 2) the software needed to post-process the output files (i.e., to analyze and visualize the simulation), and 3) the high-performance computing hardware where the models are run. We aim to match the initial conditions of our simulations to those constrained by observational evidence.

3.1.1. Computational Requirements

The complexity of the astrophysics phenomena, which we want to simulate, demands using high-performance computing. This is because we must solve all the hydrodynamics equations with a good grid resolution. To achieve this, we must run our simulation using a multiple-processor CPU-based configuration integrated with the Message Passing Interface (MPI) library for parallel computing. We perform our simulation on **SuperMUC-NG**, which is a high-performance computing facility operated by the Leibniz Supercomputing Centre (LRZ) in Germany. We conducted different three-dimensional simulations that demanded the use of 960 cores (CPUs) for all resolutions for several hours. Additionally, the computational cost changes depending on the resolution. The analysis of the output files from the simulations was carried out using Python algorithms using multiprocessing to minimize the computational cost and reduce analysis time. We store all the output project data in HPC facilities and personal storage.

3.1.2. Software

To perform numerical simulations where two clouds collide in the interstellar medium, we require specific software that allows us to set up the conditions for our simulations and evolve the hydrodynamical equations for mass, momentum, and energy conservation. This software is the PLUTO code, which is described next. For analyzing the simulation, we use Python

- **PLUTO**

PLUTO (The PLUTO Code for Astrophysical GasDynamics⁵⁴) is a numerical tool highly used in the astrophysics community due to its capability to simulate the dynamics of the gas in astrophysical environments under different conditions. It is a freely accessible package to solve different sets of hyperbolic and parabolic differential equations describing astrophysical gas dynamics. PLUTO provides different approaches to solving conservation law systems by numerical algorithms built upon Godunov-type schemes. These approaches might be finite volume or finite difference. PLUTO has four different physical modules: hydrodynamics (HD), magneto-hydrodynamics (MHD), relativistic hydrodynamics (RHD), and relativistic magneto-hydrodynamics (RMHD), which can be used depending on the context we are working on. PLUTO's adaptability allows it to simulate different astrophysical scenarios such as star formation, galactic winds, cloud collision, and shock wave interaction. The program was developed with the programming language C, but it also presents a friendly user interface to set up problems based on Python. Another important characteristic of this package is the versatility to perform calculations. PLUTO can be run on a single workstation or on facilities with hundreds of processors, such as supercomputers, owing to its parallelization with (MPI).

- **Python**

Python is a programming language highly used in the scientific community due to its versatility and diverse applications. One of the most critical applications is data analysis which makes it the best for our research purpose. We used Python to postprocess the PLUTO data via our shock-finding program developed in this programming language. The program used several Python libraries for data reading, analysis, plotting, and saving data treating. The libraries used are PyVista⁵⁵, NumPy⁵⁶, pandas⁵⁷, and matplotlib⁵⁸.

3.2. Setup of Our Numerical Simulations

In this section, we explain the setup of the numerical simulations, including the most important parameters.

3.2.1. Polytropic Index, γ

The polytropic index γ plays an essential role in our simulation because it defines the thermodynamics of the equation of the state of the gas in the colliding clouds. Additionally, it influences shock propagation and evolution

across the clouds because it describes the nature of the gas in our simulation. We consider a quasi-isothermal $\gamma = 1,01$ to mimic the conditions existing in interstellar molecular gas.

3.2.2. Mean Particle Mass, μ

The mean particle mass (μ) is used in astrophysics to study the chemical composition of different clouds. It is essential because of the relation between the chemistry of the cloud and the thermodynamic effects it creates. It is computed using the fraction of each element present in the medium (x_i), the atomic weight (A_i), and the number of protons (Z) related to the following equation:

$$\frac{1}{\mu} = \sum \left(\frac{x_i}{A_i} (1 + Z) \right) \quad (3.1)$$

We interested in molecular gas and its thermodynamical properties (density, pressure and temperature depend on μ), so we use a $\mu = 2,36$ considering the composition of a typical molecular cloud (with a composition of 71 % Hydrogen 27 % Helium, and 2 % Metals). For our work, we consider that all hydrogen H in the cloud is H_2

3.2.3. Larson Laws

Larson's laws are empirical astrophysical laws for molecular clouds that are based on observational data. The laws provide estimates that can be used as constraints in computational and theoretical physics models. Three different Larson's laws relate to some properties of molecular clouds.

- **Turbulence law:** This relates the velocity dispersion σ as a function of the cloud size L .

$$\sigma \left(\text{km s}^{-1} \right) = 1,10 L \text{ (pc)}^{0,38} \quad (3.2)$$

which implies that as we increase the size of the cloud, the turbulence also increases.

- **Gravity law :** The second law relates the velocity dispersion σ and the cloud mass M .

$$\sigma \left(\text{km s}^{-1} \right) = 0,42 M \text{ (M}_\odot\text{)}^{0,20} \quad (3.3)$$

- **Density law:** The last Larson law relates the number density $n(H_2)$ and the cloud size M . This relation is inversely proportional.

$$\langle n(H_2) \rangle \text{ (cm}^{-3}\text{)} = 3400 L \text{ (pc)}^{-1,10} \quad (3.4)$$

We can derive a new law connecting the cloud size and mass using the two first laws and obtain the following combined equation:

$$L \text{ (pc)} = \left(3,82 * M \text{ (M}_\odot\text{)}^{0,2} \right)^{2,632} \quad (3.5)$$

The initial conditions must satisfy equation 3.4, 3.5 to constrain our simulations to observational laws. Figure 3.1, and Figure 3.2 show the observational law in the blue line, while the green and yellow diamonds show the initial values for the Habe Ohta model and the identical cloud model, respectively. Also, both figures show that our model successfully satisfies equations 3.4 and 3.5.

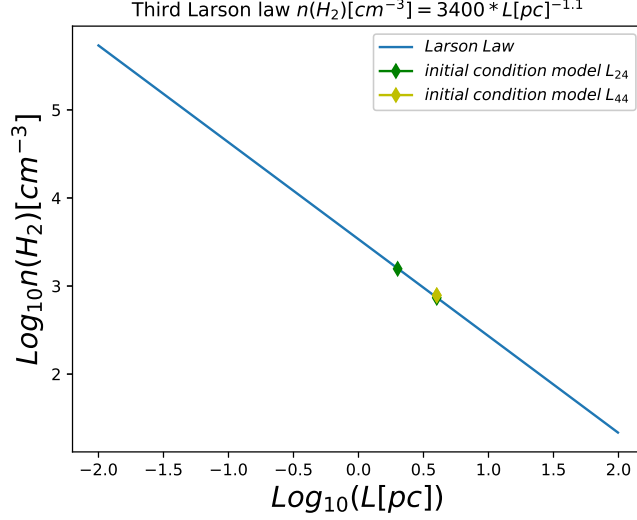


Figure 3.1: Third Larson’s law: relates the number density compared as a function of the cloud size (diameter). The blue line represents the values that Larson’s law may take for different masses. The green and yellow diamonds show the initial condition for the Habe Ohta model and the identical cloud model, respectively.

3.2.4. PLUTO set-up

We perform our simulations of cloud-cloud collisions using the last version of PLUTO $v4.4^{54}$. All our models were performed using the hydrodynamics module in a 3D Cartesian coordinate system (X, Y, Z). The hydrodynamic module solves all hydrodynamics equations where the mass, momentum, and energy conservation equations are 3.6, 3.7, and 3.8, respectively.

$$\frac{\partial \rho}{\partial t} + \vec{\nabla} \cdot [\rho \mathbf{v}] = 0 \quad (3.6)$$

$$\frac{\partial \mathbf{m}}{\partial t} + \vec{\nabla} \cdot [\mathbf{m} \mathbf{v} + P \mathbf{I}] = 0 \quad (3.7)$$

$$\frac{\partial E}{\partial t} + \vec{\nabla} \cdot [E + p \mathbf{v}] = 0 \quad (3.8)$$

where ρ is mass density, the momentum is define as $\mathbf{m} = \rho \cdot \mathbf{v}$, p is thermal pressure, \mathbf{I} is the identity matrix, \mathbf{v} is velocity, E is the total energy density.

These are volumetric equations. ρ is in function of the atomic mass unit m_μ , mean particle mass μ , and number density n . It is defined as $\rho = \mu m_\mu n$. The hydrodynamic module also implements the ideal equation of state as a function of the polytropic index γ , density ρ , and the gas internal energy ϵ .

$$P = (\gamma + 1) \rho \epsilon \quad (3.9)$$

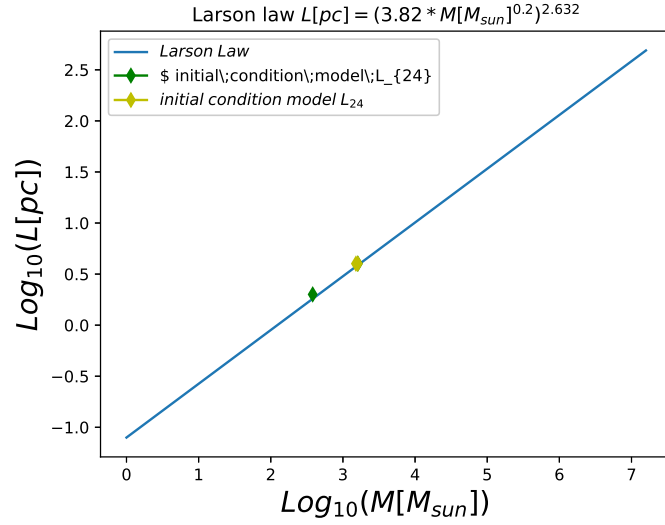


Figura 3.2: Larson's law: obtained from the first and the second Larson's law, which relates the cloud size (diameter) with the cloud mass. the blue line represents the values that Larson's law may take for different masses. The green and yellow diamonds show the initial condition for the Habe Ohta model and the identical cloud model, respectively

Where the polytropic index was defined as $\gamma = 1,01$ for our simulations. In order to trace the motion of the two clouds, we used the following advection equation:

$$\frac{\partial \rho C}{\partial t} + \vec{\nabla} [\rho C v] = 0 \quad (3.10)$$

C takes values of 1 for material inside the cloud and 0 for outside. Additionally, for solving the system of the hyperbolic differential equation, we configured the PLUTO code with TDVLF solver, which uses the Lax-Friedrich method. This solver is robust because it prevents the presence of negative pressures and densities that can create numerical instabilities causing the simulation to diverge or a non-physical result. For the time discretization method, we used a second-order Runge-Kutta method (RK2). An important remark about this solver is that it makes our simulations more diffusive. However, it is recommended by the PLUTO developers for simulations that would present high Mach numbers or high-pressure gradients.

3.2.5. Initial and Boundary Conditions

Our simulation involves the collisions of two clouds where one of the clouds is moving with respect to the other one with a certain velocity. For this, we use two different models the Habe-Ohta model, where the moving cloud is small compared with the initially non-moving cloud, and the identical cloud model, where the two clouds have the same size. Our simulations domain consists of a box of 20 pc^3 with a resolution of 128 cells for each size with width, length, and height denoted as X, Y, Z .

The boundaries of the simulations were set up as follows:

- $X_{beg} = -7,5$ pc and $X_{end} = 12,5$ pc
- $Y_{beg} = -10$ pc and $Y_{end} = 10$ pc
- $Z_{beg} = -10$ pc and $Z_{end} = 10$ pc

The initial position of the clouds was established as follows the center of the initially non-moving cloud is located in (0,0,0) while the center of the other cloud is located such that the border of the two clouds is separated by 1pc (see Figure 3.3).

The boundary conditions for our simulations were configured as outflow conditions for all sides, which makes zero gradients when the flow crosses boundaries.

$$\frac{\partial q}{\partial n} = 0 \quad (3.11)$$

$$\frac{\partial v}{\partial t} = 0 \quad (3.12)$$

where q are studied variables. Outflow conditions force the gas to go out of the computational domain.

We run different simulations, changing their initial conditions, such as cloud size and collision velocity (see table 3.2.5). The first group in the table varied the cloud size to analyze the influence of this parameter on the evolution of cloud and the the creation of shocks.

Cuadro 3.1: Initial conditions in our simulation set. Cloud 1 represents the moving cloud, while Cloud 2 shows values for the initially non-moving cloud.

Simulation ID	Cloud Diameter		Cloud Initial Velocity		Polytropic Index
	Cloud 1 pc	Cloud 2 pc	Cloud 1 km s ⁻¹	Cloud 2 km s ⁻¹	γ
m24_v030 *	2	4	20	0	1.01
m44_v030	4	4	20	0	1.01
m24_v020	2	4	20	0	1.01
m24_v050	2	4	50	0	1.01
m24_v070	2	4	70	0	1.01
m24_v090	2	4	90	0	1.01

The second group studies the distribution of the shocks as a function of the collision velocity. The velocities varied on a range from 20 km s⁻¹ to 90 km s⁻¹ where one of the clouds is moving with respect to the other with the collision velocity while the other is not moving. We define these velocities considering the gas velocities in different regions of the Galaxy.^{2,59,60}

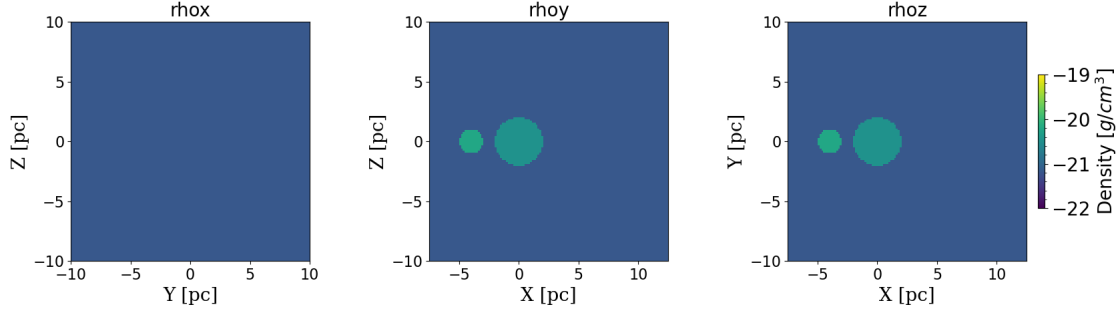


Figura 3.3: Maps of 2D slices at $X=2.5$ [pc], $Y=0$ pc and $Z=0$ pc of density at time $t = 0$ in the standard model ($m24_v030$ s). The small denser cloud is the cloud that is moving, and the larger cloud is the initially non-moving cloud. The color bar is in logarithmic scale

3.2.6. Diagnostics

To study the collision of two clouds and analyze their evolution, some integral quantities must be calculated from the simulated data. These quantities are the mass-weighted velocity, volume-weighted velocity, center of mass of the clouds, and the cloud mass. We used the following equations to calculate the different integral quantities.

$$\langle F \rangle = \frac{\int \rho C F dV}{\int \rho C dV} \quad (3.13)$$

$$[G] = \frac{\int C G dV}{\int C dV} \quad (3.14)$$

$$\langle r \rangle = \frac{\int \rho C r dV}{\int \rho C dV} \quad (3.15)$$

Where $\langle F \rangle$ is the mass-weighted average of the variable F , C is the cloud tracer, V is the volume, $[G]$ is the volume weighted average of the variable G , $\langle r \rangle$ is the center of mass. All of these quantities provide information on the time evolution of the simulation. Additionally to these quantities, we calculate the mean density $[\rho]$, mean pressure $[p]$, mean temperature $[T]$, and mean velocity dispersion $[\sigma]$.

3.3. Data Analysis

Once we run our numerical simulation with PLUTO⁵⁴, the output files are written as VTK files containing the result of our initial conditions. Our simulation consists of 100 snapshots in time (so we have 100 VTK files). For analyzing the VTK files, we used the Python script to analyze these files with our shock-finding program. We run our shock-finding script for processing the data on **SuperMUC-NG**.

3.3.1. Shock detection algorithm

The VTK files, containing the information of the variables of interest were read using the Pyvista library. The data of the different variables are then saved as 3D arrays.

The variables from the VTK files are :

- Density ρ
- Thermal Pressure P
- Velocity $\vec{v} = (v_x, v_y, v_z)$
- Tracer of the gas of each of the two clouds: the moving cloud and the initially non-moving cloud

The tracer helps to understand each cloud's behavior, evolution, and gas interaction. Once the data are saved in several arrays, we calculate some other variables from input variables, such as the temperature 3.16, sound speed 2.16, and speed $|\vec{v}|$.

$$T = \frac{P}{\rho} \quad (3.16)$$

It is important to mention that all of the variables are in code units. We multiplied the normalization units (see Appendix A) by the different 3D arrays containing data information. After normalization, the initial conditions are summarized in table 3.2.

Cuadro 3.2: Initial condition of the different variables analyzed. Cloud 1 represents the moving cloud, while Cloud 2 shows values for the initially non-moving cloud.

Simulation ID	Pressure		Density		Temperature		Mass		Sound Speed	
	K cm ⁻³		g cm ⁻³		K		M _⊙		km s ⁻¹	
	Cloud 1	Cloud 2	Cloud 1	Cloud 2	Cloud 1	Cloud 2	Cloud 1	Cloud 2	Cloud 1	Cloud 2
	×10 ⁴	×10 ⁴	×10 ³	×10 ²			×10 ²	×10 ³	×10 ⁻¹	×10 ⁻¹
m24_v030 *	3.13	3.13	1.57	8.33	19.95	37.60	3.81	1.61	2.70	3.70
m44_v030	3.13	3.13	0.78	8.33	39.90	37.60	15.14	1.61	3.80	3.70
m24_v020	3.13	3.13	1.57	8.33	19.95	37.60	3.81	1.61	2.70	3.70
m24_v050	3.13	3.13	1.57	8.33	19.95	37.60	3.81	1.61	2.70	3.70
m24_v070	3.13	3.13	1.57	8.33	19.95	37.60	3.81	1.61	2.70	3.70
m24_v090	3.13	3.13	1.57	8.33	19.95	37.60	3.81	1.61	2.70	3.70

- The duration of all simulations is $t = 2$ Myr.

After normalizing the different variables, our program computes integrated quantities and searches for shocked cell candidates. First, our routine computes the pressure gradient for each cell. Then it calculates velocity divergence by searching for convergence flows. The cells that achieve both conditions are tagged as candidates to be shock waves

and are used to create binary maps. Then, the algorithm calculates the shock Mach number in each of the cells using equation 2.17. After calculating the Mach number, we search for the center of the shock using the function *peak_finder()* contained in the library *scipy.signal* once we find the maximum value and return its cells with a value of 1 while setting the neighbor unshocked cells at 0. Afterward, the resulting array from the *peak_finder()* is multiplied by the calculated Mach numbers in order only to have shocked cells. After, we plot the slices of Mach numbers and shock histograms. Figure 3.4 represents the flow chart of our program.

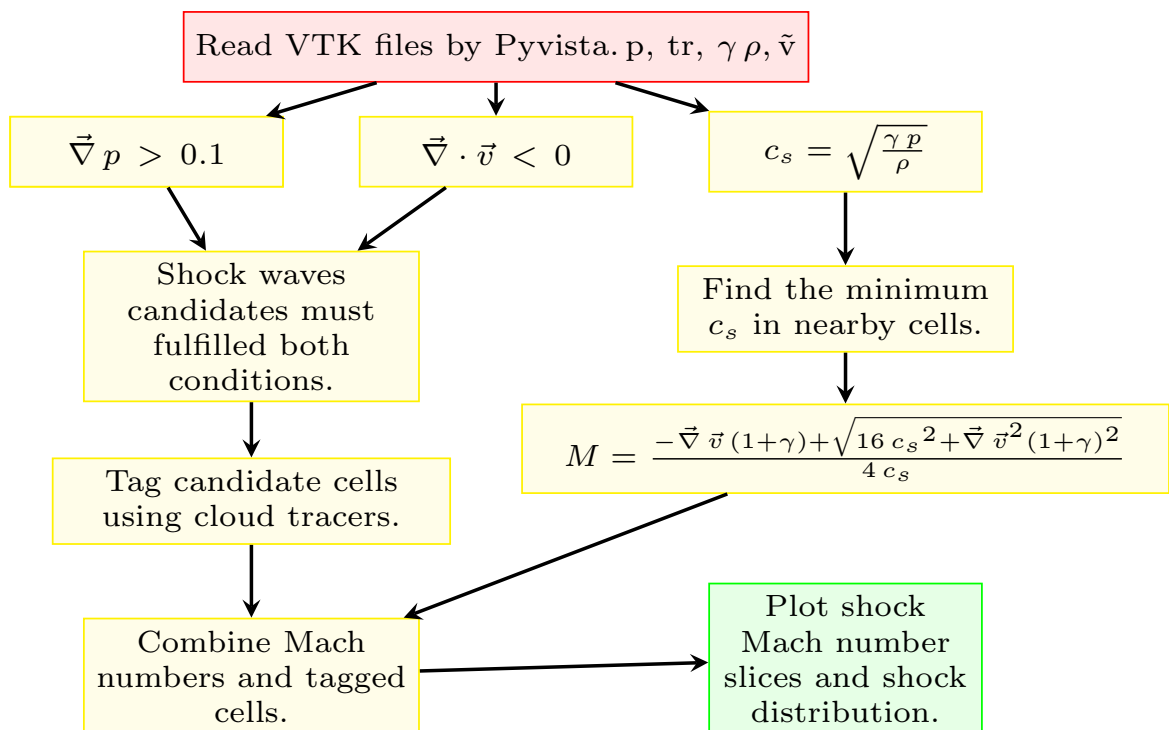


Figura 3.4: Flowchart of how our shock-finding algorithm works. The input files are VTK files, and the output files are images showing the shock Mach numbers.

Capítulo 4

Results & Discussion

4.1. Evolution of interstellar cloud-cloud collisions

Figures 4.1, 4.2, and 4.3 show the temporal evolution of the gas density, temperature, and pressure, respectively, into two-dimensional slices at different times of our standard model m24_v030 (see table 3.2.5). The panels are organized into rows presenting slices at the same time, while the columns show the same slices at $X = 2,5$ pc, $Y = 0$ pc, and $Z = 0$ pc, respectively. These panels correspond to the standard model with a collision velocity of 30 km s^{-1} . We chose this as the standard model because the literature suggests that the typical collision velocity of CCc simulations in our galaxies occurs at this velocity.^{61 39 62} The evolution of CCc can be characterized by 3 different stages, as proposed in the Habe-Ohta model. However, in our case, we consider the first two stages (Stage I and Stage II) as they are a part of the same physical process. The top panels of Figures 4.1, 4.2, 4.3, show the initial conditions of the simulation in which the smaller cloud is denser than the larger one owing to the Larson laws described previously. The next panels of this figure illustrate the following stages of CCc evolution.

- **Pre-collision stage.** The variables of the moving cloud change from the beginning of the simulation because of the interaction of the cloud with the surrounding medium as it moves. This interaction creates Kelvin-Helmoltz instabilities at the boundaries between the cloud and the ambient medium, which cannot be clearly seen at small scales in this simulation due to the resolution.
- **The first stage, compression stage** (see Figure 4.1, 4.2, and 4.3 second row), is characterized by the initial interaction between the small cloud (moving cloud) and the second cloud (initially non-moving cloud) at a time of 0.156 Myr. At this time, the first layers of the initially non-moving cloud start to compress and create internal shocks in the initially non-moving cloud and also in front of the smaller moving cloud. Also, we can see that the back of the moving cloud creates a region with low densities. This is known as a rarefaction zone which is a region of relatively low densities and pressure behind the shock region. It is produced by the motion of the cloud, which compresses the gas of the initially non-moving cloud. Another characteristic of this stage

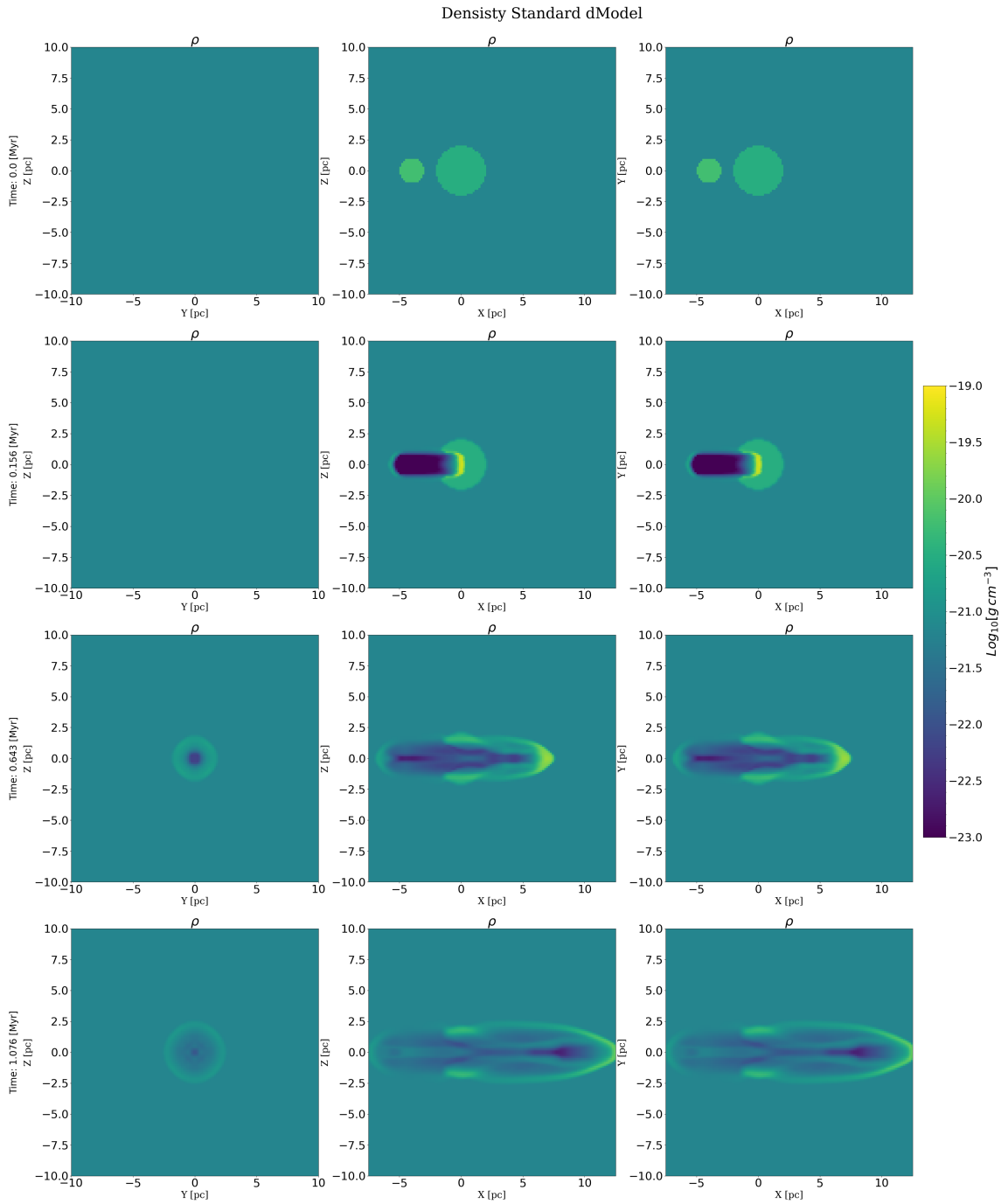


Figure 4.1: Density maps of different panels at different times in cloud collision. The left panels show slices at $X = 2.5$, the middle panels at $Y = 0$, and the right panels slice at $Z = 0$. The color bar is in a logarithmic scale.

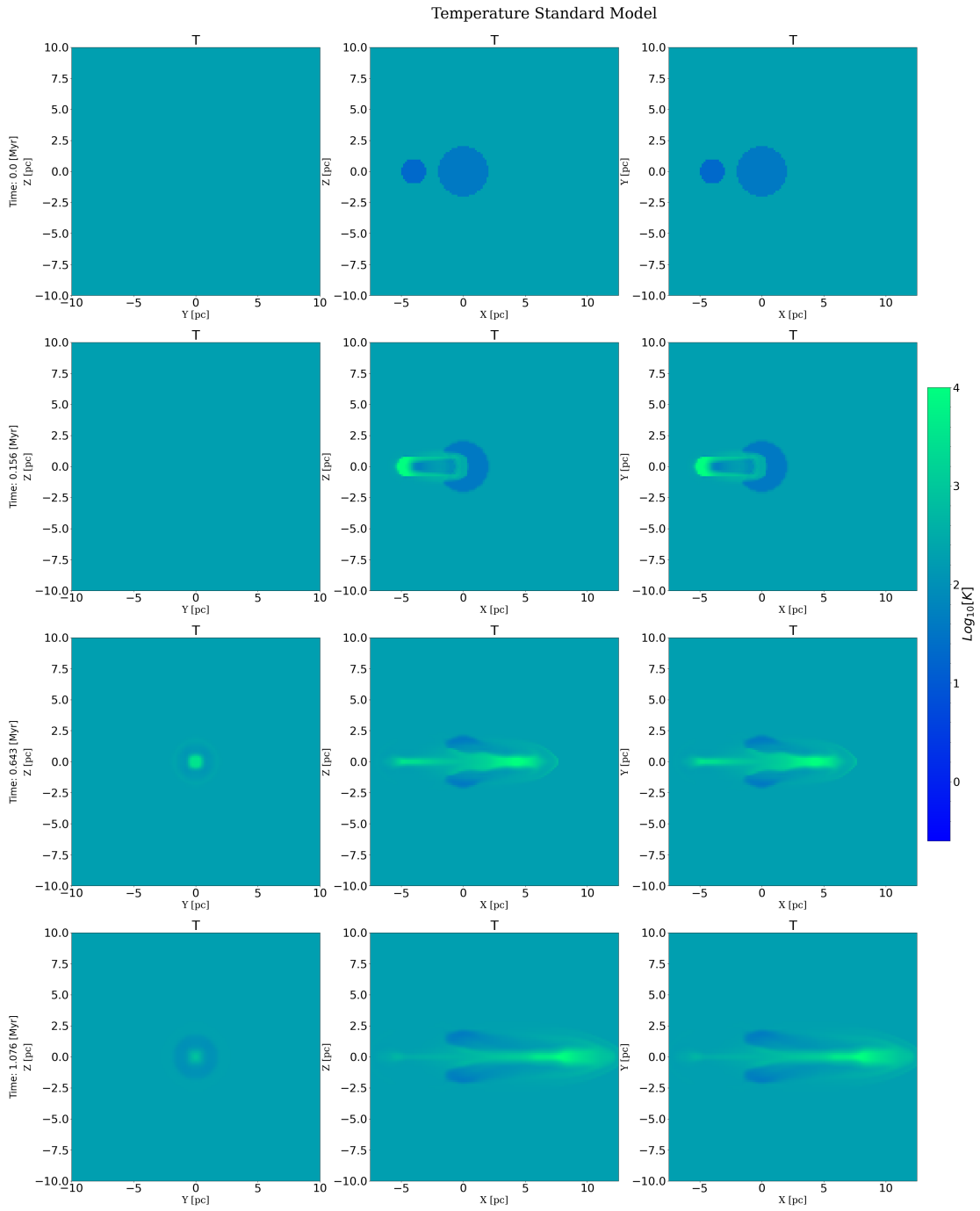


Figure 4.2: Temperature maps of different panels at different times in cloud collision. The left panels show slices at $X = 2.5$, the middle panels at $Y = 0$, and the right panels slice at $Z = 0$. The color bar is in a logarithmic scale.

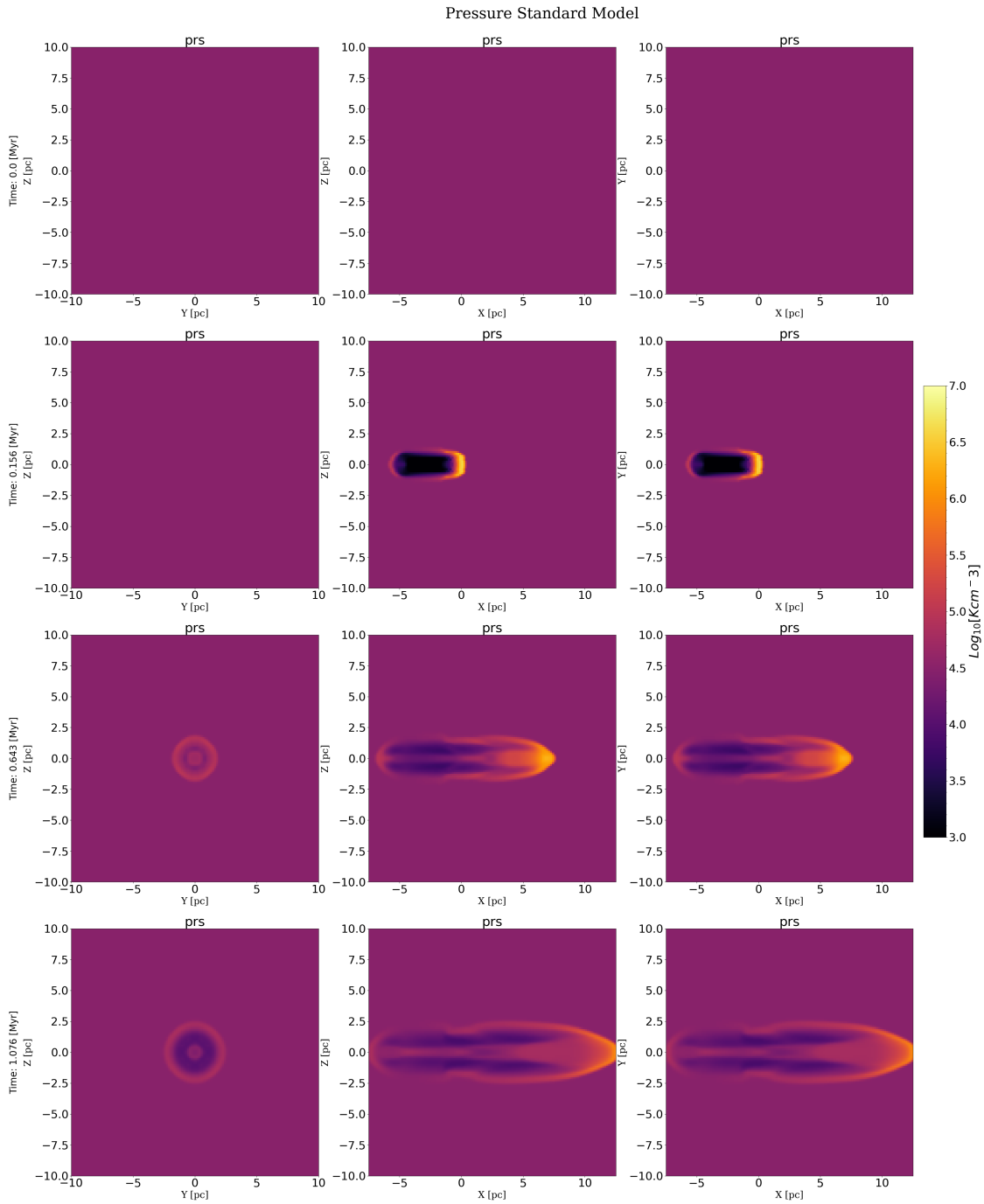


Figure 4.3: Pressure maps of different panels at different times in cloud collision. The left panels show slices at $X = 2.5$, the middle panels at $Y = 0$, and the right panels slice at $Z = 0$. The color bar is in a logarithmic scale.

is the increase in temperature and pressure of the colliding clouds and the surrounding medium. This creates the characteristic U shape of the Habe-Ohta model.

This feature can be corroborated by looking for the evolution of the average integrated variables presented in Figure 4.4. In that Figure, the mean number density is shown in panel A, which shows that there is a decrease in densities of the moving cloud and not much difference in the initially non-moving cloud. The thermal pressure (panel B) also increases drastically in the colliding cloud. Even when the interaction starts, the average pressure for the larger cloud also increases, but not as much as the moving cloud. The temperature (panel D) and sound speed (panel E) of both clouds exhibit the same behavior as thermal pressure. The median Mach numbers (panel F) are higher in both clouds at the beginning of their initial interaction, indicating that stronger shocks form only at the early stages of the CCs. The moving cloud in red in Figure 4.4 presents a higher shock Mach number when the simulation starts due to the initial motion, but after the interaction between the two clouds starts, the initially (non-moving) cloud presents an increase of the median Mach number until reaching a peak followed by a sharp decrease, which indicates that the strongest shocks dissipate shortly after they are created. The moving cloud exhibits the same behavior but with a lag in time.

- **Second stage, pass-through stage** (see Figure 4.1, 4.2, and 4.3 third row). The evolution of the interaction of the two clouds at this time has reached a point where the colliding cloud has passed through the initially non-moving cloud. The time of this slice is 0.643 Myr. The main characteristic of this stage is the formation of the bow shock in front of the moving cloud and the presence of back-flows in the rarefaction zone produced by the material stripped from both clouds, which starts to move to this region. Also, most of the stronger shocks can be detected along the bow shocks. Notice that the biggest differences in pressure and densities are in the borders of the perturbations. At this stage, all the studied variables reach their minimum or maximum values because the moving cloud's gas has moved through the second cloud and triggered an expansion of the gas. The majority of the shocks can be found at this stage. The U shape inside the initially non-moving cloud remains, but the U shape is extended and deformed. Also, the presence of the Mach cone at the back of the moving cloud is more evident at this stage. At this time, the dissipation via shocks becomes important, which is reflected in the decrease in the median Mach number, which converges to a characteristic Mach number $M \approx 1.7$.
- **Final stage, dissipation stages** (see Figure 4.1, 4.2, and 4.3 bottom rows). This stage corresponds to the processes where the shocked gas from both clouds propagates and interacts with the ambient ISM. It can be seen in all the figures where the intensity of the color decreases. The Mach cone has evolved and clearly can be seen in the low-density region behind the bow shock. The trends of the studied variables relax and converge to certain values (Figure 4.4). However, we cannot study any possible later stages of evolution because after the gas flow gets to the boundary, due to the size of the box, we lose the mass of both clouds, and this creates a bias in the results. The point at which the exit of the material from the computational domain starts to occur is shown in grey in Figure 4.4. Another important remark is that at this stage, the dissipation process is controlled by turbulent dissipation at small subsonic eddies rather than at shocks, as most strong shocks have vanished. Many dissipation processes can take place once cloud collisions occur. The most characteristic is the thermal

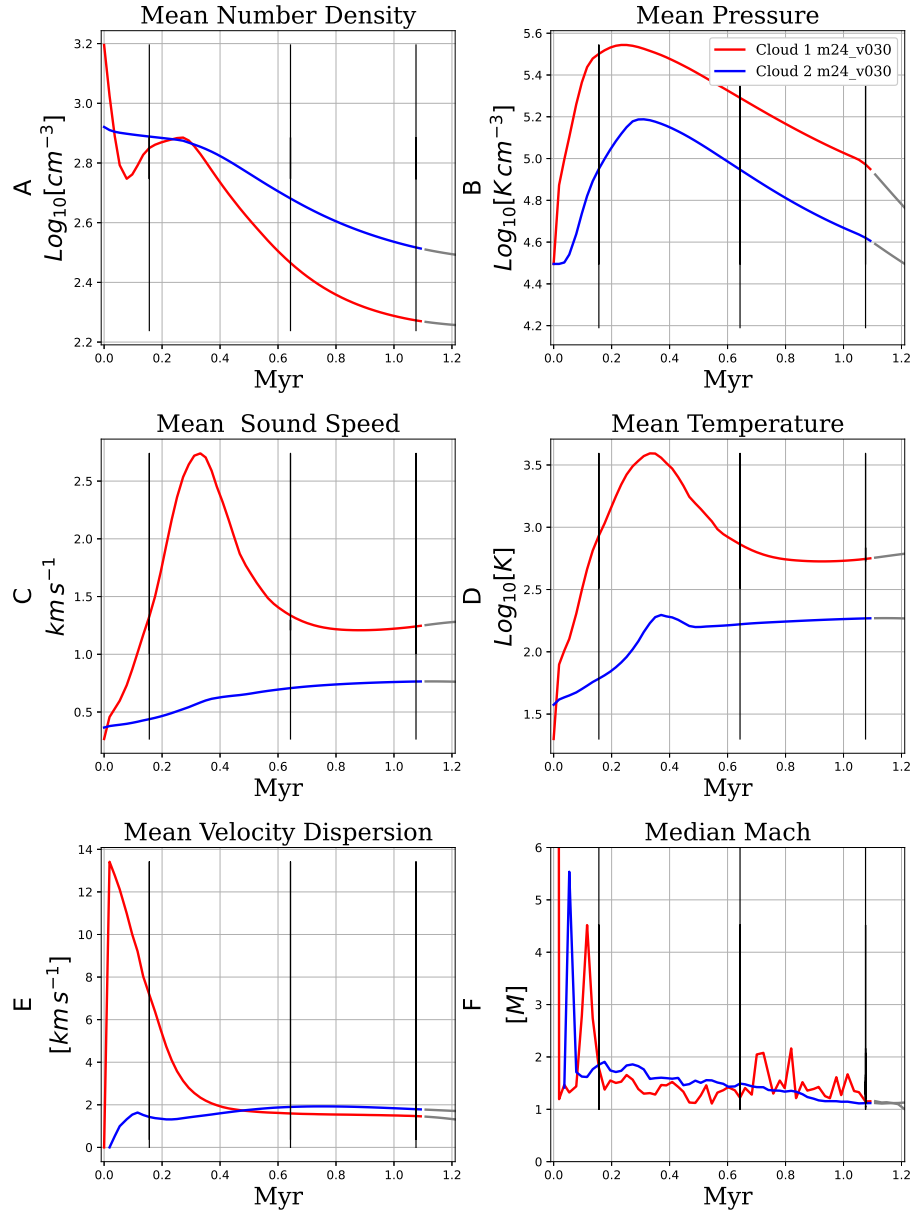


Figure 4.4: Diagnostics curves of the evolution of the colliding clouds. Panel A shows the average number density n . Panel B displays the average thermal pressure. Panel C shows the average sound speed, while panel D shows the average temperature. At the bottom panels, we can find the average velocity dispersion (panel E) and median Mach number (panel F). The moving cloud is shown in red, while the initially non-moving cloud is shown in blue. The black lines mark the times that are represented in Figures 4.1-4.3.

dissipation via shocks and turbulence. The collision produces thermal dissipation because it generates shocks at early stages and produces an increase in temperature accompanied by the compression of the gas in the surroundings of the hot shocked region. Even though we are not using initially turbulent clouds for the collision, the collision by itself can generate turbulence inside the clouds that will create a cascade where the energy is transferred from the large scales to smaller scales heating up the gas. The characteristic form of turbulent instabilities is cloud fingers or spikes⁶³, which arise in density maps. In addition, panel F of Figure 4.4 shows that at this stage, the mean Mach number has reached its characteristic Mach number for the standard model, which is around $M \approx 1.5$. Another important characteristic of our simulation is that the larger cloud, initially a non-moving cloud presents supersonic turbulence, shown by the M_{rms} (equation 2.22). M_{rms} is greater than 1 during the whole simulation. However, the colliding cloud is supersonic for most of the simulation, with the exception of a period around (0.30-0.40) Myr when it becomes subsonic, and after this period, it comes back to its initial supersonic behavior.

In the final stage of the collision evolution, the cloud reaches the boundary, so cloud material exits the computational domain, and we lose most of the shocks and dynamical information after this time. It is important to mention that the results presented here are shown for times at which less than 25 % of the mass of the colliding cloud has left the box, so the results are still reliable and unbiased. The diagnostic curves, depicted in grey, indicate the time at which the mass of the clouds exits the computational domain.

4.2. On the effect of cloud size

Figure 4.5 presents slices of density for our standard model (*m24_v030*) with a small and a large cloud, and identical cloud model (*m44_v030*) with two equally -sized clouds, at the same time ($t = 0.45$ Myr). The top row presents the standard model, the bottom row presents the model with clouds of the same size. This figure's state of evolution corresponds to the second stage described in the previous section. At this point of the collision evolution, for the standard model, the small moving cloud has passed through the second larger cloud and has created the U shape characteristic of the Habe-Ohta model. Most of the gas of the second cloud has been compressed and has already interacted with gas from the colliding cloud.

Given the large cloud size, the identical cloud model produces a different behavior than the standard model. The collision cross-section for this case is larger, which facilitates higher gas interaction between the two clouds. This means that the amount of gas affected by the collision is volumetrically larger than in the standard model. In the identical cloud model, the U shape is larger and presents diffuse wakes produced by the gas expansion. U shape in the standard model is narrow, and it has a thin foot point just behind the shock region. Additionally, the wakes for this model are thick and dense. The complete destruction of both clouds can be seen in 4.5 in concordance with previous work.³⁷ The increase in temperature in the moving cloud is relatively similar for both models, however, the initially non-moving cloud exhibits a higher increase in temperature compared with the standard model.

The formation of the Mach cone can also be more evident for the identical cloud model, but the amount of gas in the rarefaction region is lower than in the standard model, which makes it a lower-density region.

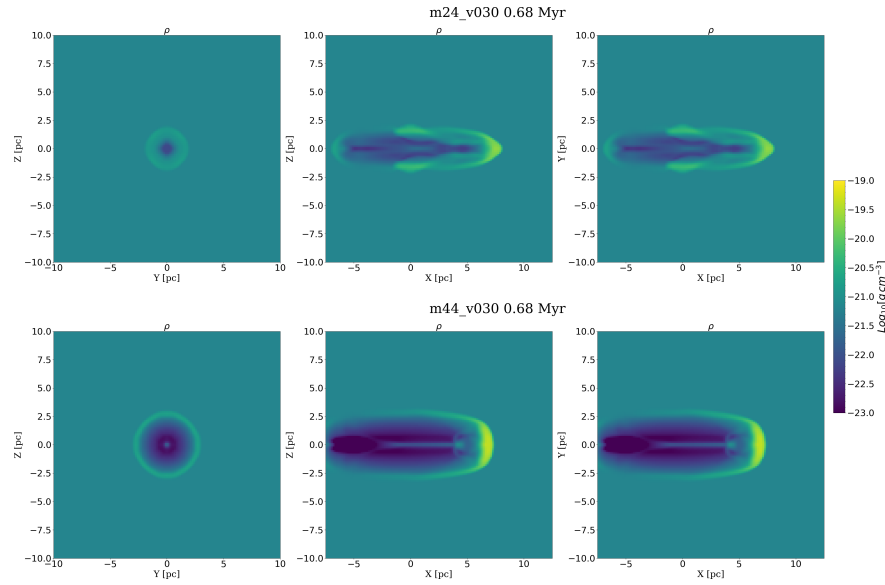


Figure 4.5: Density maps on different planes. The color bar is on a logarithmic scale. Top row Standard model where clouds of different sizes, bottom row identical cloud model two clouds of the same size are colliding

Figure 4.6 shows the diagnostic properties comparing the identical cloud model (dashed lines and the standard model (solid lines), which describe the evolution in time of the most important physical properties. The top panels show the densities and pressures, where the density of the initially non-moving cloud for the identical cloud model suffers an abrupt density drop given the large amount of the affected area and volume compared with the standard model, which looks like the initially non-moving cloud got destroyed, and the moving cloud is the only one left. The amount of gas affected produces a greater increase in pressure due to the large collision cross-section. There is also a more evident increase in sound speed and temperature in the initially non-moving cloud, while the moving cloud has higher values for the standard model as it is being affected by the gas of the bigger cloud that develops the U cavity.

The last two panels show the velocity dispersion and the median Mach numbers. The left panel shows that the turbulence inside the two clouds produced by the collision is more significant than the identical cloud model's moving cloud. The moving cloud for the identical cloud model does not have the same behavior as the standard model because it does not return to supersonic turbulence with $M_{rms} < 1$. The right panel reveals that stronger shocks are present in the second initially non-moving cloud of the identical cloud model, which reaches values bigger than $M = 100$ at the initial stages of the collision, but the moving cloud presents higher values for the standard model because the moving cloud's edge has more interaction with the gas of the initially non-moving cloud. Even though both models present the same characteristic median Mach number at the final stage of the simulation, their difference is expressed in their characteristic turbulence velocities and M_{rms} , which present higher M_{rms} for the standard model.

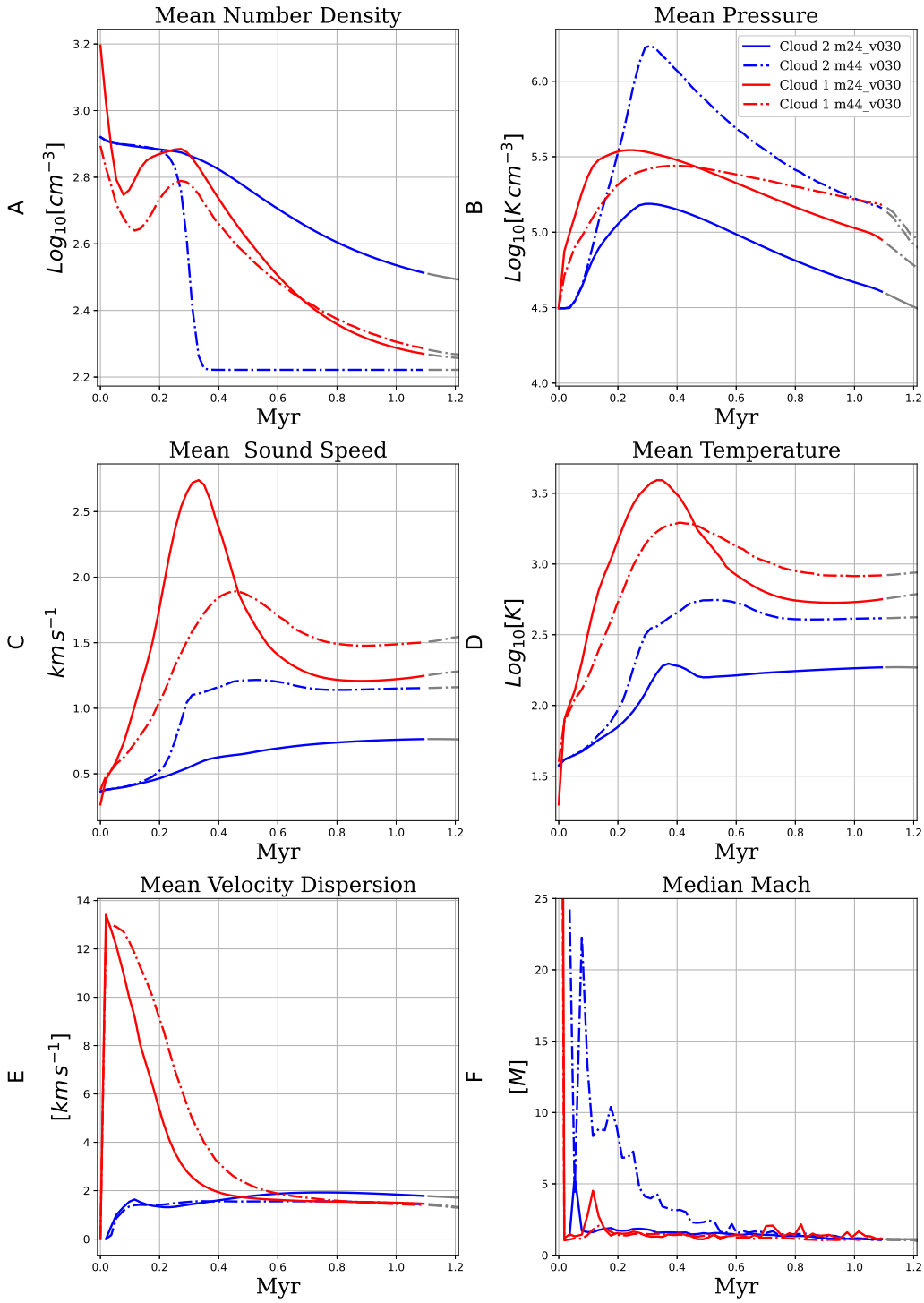


Figure 4.6: Diagnostics curves of the moving cloud at the evolution of cloud collision varying the size of the moving cloud. The number density n is shown in panel A, the pressure on panel B, on the middle panels on left sound speed (panel C), while panel D shows temperature, the velocity dispersion (panel E), and median Mach number (panel F). Labels are presented in panel B, where the standard model is present in solid line, and clouds of diameters of 2 pc and 4 pc are shown in red and blue, respectively.

4.3. On the effect of varying the collision velocity

Figure 4.7 shows slices of the density of models with different collision velocities at the same time $t = 0,68\text{Myr}$. The top row of this figure illustrates the standard model ($m24_v030$), while the others are depicted below for increasingly higher velocities. For collision velocities of 30 km s^{-1} and 20 km s^{-1} , the collision evolution is in the second stage where the gas of the moving cloud affects the gas of the larger cloud, while for higher velocities, the collision is at dissipation stage as these models evolve faster owing to the higher velocities. Looking at these panels, the most obvious interpretation can be done by looking at the position of the gas at different velocities. As expected, the gas moves farther away in models with higher velocities.

All of the models present three main characteristics as displayed in figure 4.7. First is the formation of the rarefaction region created by the motion of the colliding cloud, and the other characteristic formation is the Mach cone behind the bow shock and the shocked gas. Also, notice that at this time, some material of the initially non-moving cloud around its initial position has not been moved, but its physical properties have changed. For the high-velocity collision models, two different low-density zones are inside the rarefaction regions, like two Mach cones that join each other where the initially non-moving cloud is placed. This effect is a product by the reflected shocks that are produced after the initial contact between the two clouds. Such reflected shocks move from right to left and interact in the rarefaction zone. Also, for the high-velocity collision, there is an expansion process. Another important visual characteristic is that the rarefaction region is more evident as the collision velocity increases. Additionally, as we increase the velocity, the amount of gas affected also increases.

Figure 4.8 and 4.9 present the evolution of the diagnostic of the moving cloud and the initially non-moving cloud, respectively. The first main observation is the scaling in time as we increase the collision velocities. Scaling implies that properties exhibit the same behavior as the standard model but shifted in time. Such scaling is typically found in similar models (see Banda-Barragán *et al.* 2020). Despite the scaling, we also see that densities are systematically lower as the collision velocity increases, implying further cloud destruction, while thermal pressure, sound speed, and temperature show the opposite, i.e., they are systematically higher for higher collision velocities. This suggests that high-velocity collisions inject more kinetic energy into the clouds, and this is efficiently converted into thermal energy, thus increasing gas pressure and temperature. It is essential to mention that as we increase the collision velocity to high velocities, the increase in temperature will also produce gas ionization in the colliding cloud, which reaches a temperature higher of $1 \times 10^4\text{ K}$ for colliding velocities bigger than 50 km s^{-1} . The velocity dispersion for the non-colliding cloud has the same behavior but exhibits more turbulence (see Figure 4.9). The moving cloud presents a more accentuated difference as the collision velocities increase compared to the initially non-moving cloud. In the initial stage of the collision, the velocity dispersion is systematically higher for higher collision velocities which suggests that higher collision velocities produce more turbulence at the initial stage inside the colliding cloud. It presents the same behavior as the standard model.

The panel F of Figures 4.8 and 4.9 show the median of the shock Mach number inside each cloud. The first cloud presents a median Mach number of $M \approx 3$ at the initial stages, which is characteristic of the colliding cloud in typical star formation regions of our galaxies^{2,39,48}. Notice that the first peak where the collision takes place is moving to the left, showing that the interaction between the two clouds occurs systematically earlier for higher collision velocities.

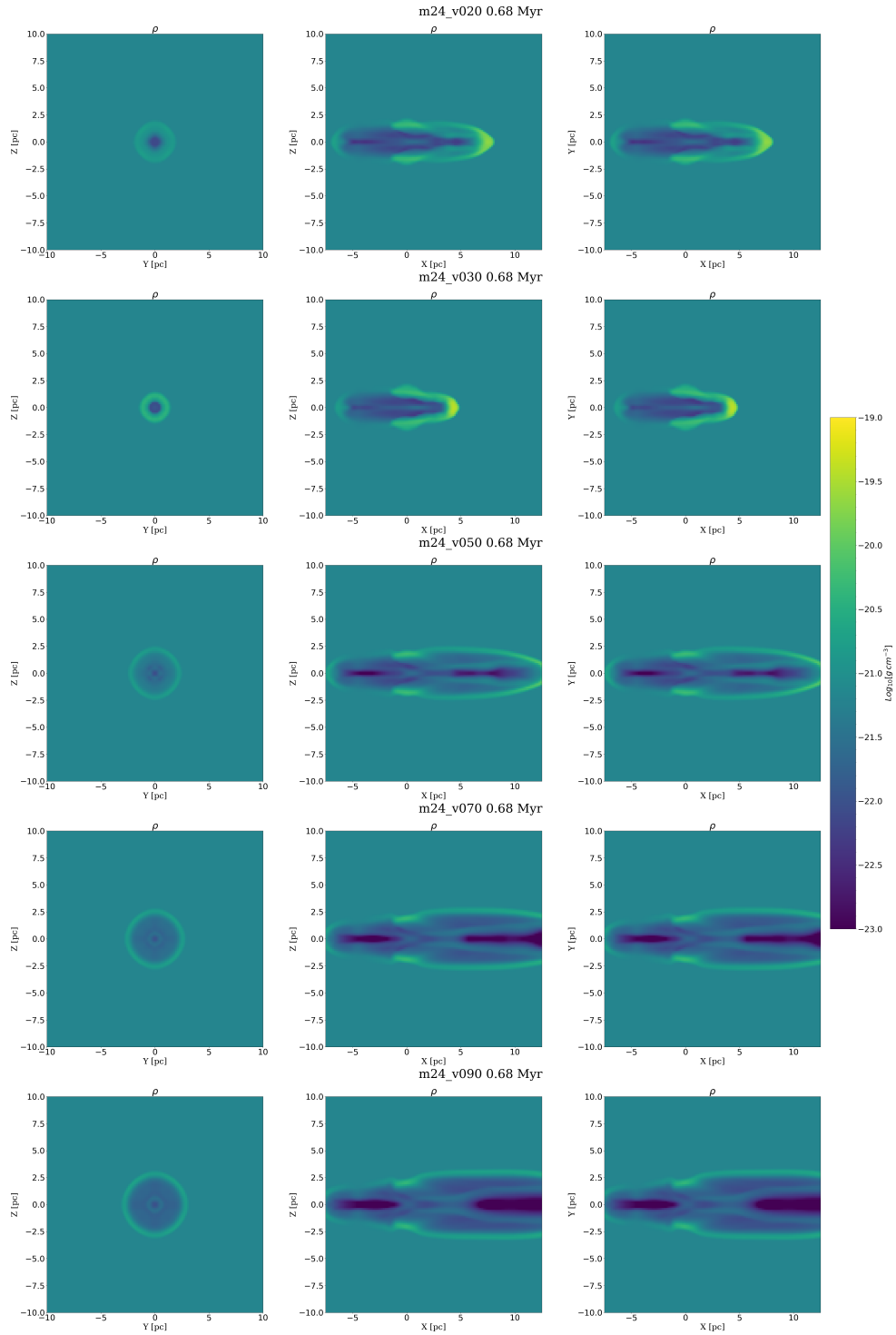


Figura 4.7: Density maps for different slices. The color bar is on a logarithmic scale. The top row is the standard model with a collision velocity of 30 km s^{-1} , while the other models have velocities of 20, 50, 70, 90 km s^{-1} from the second row to the bottom row.

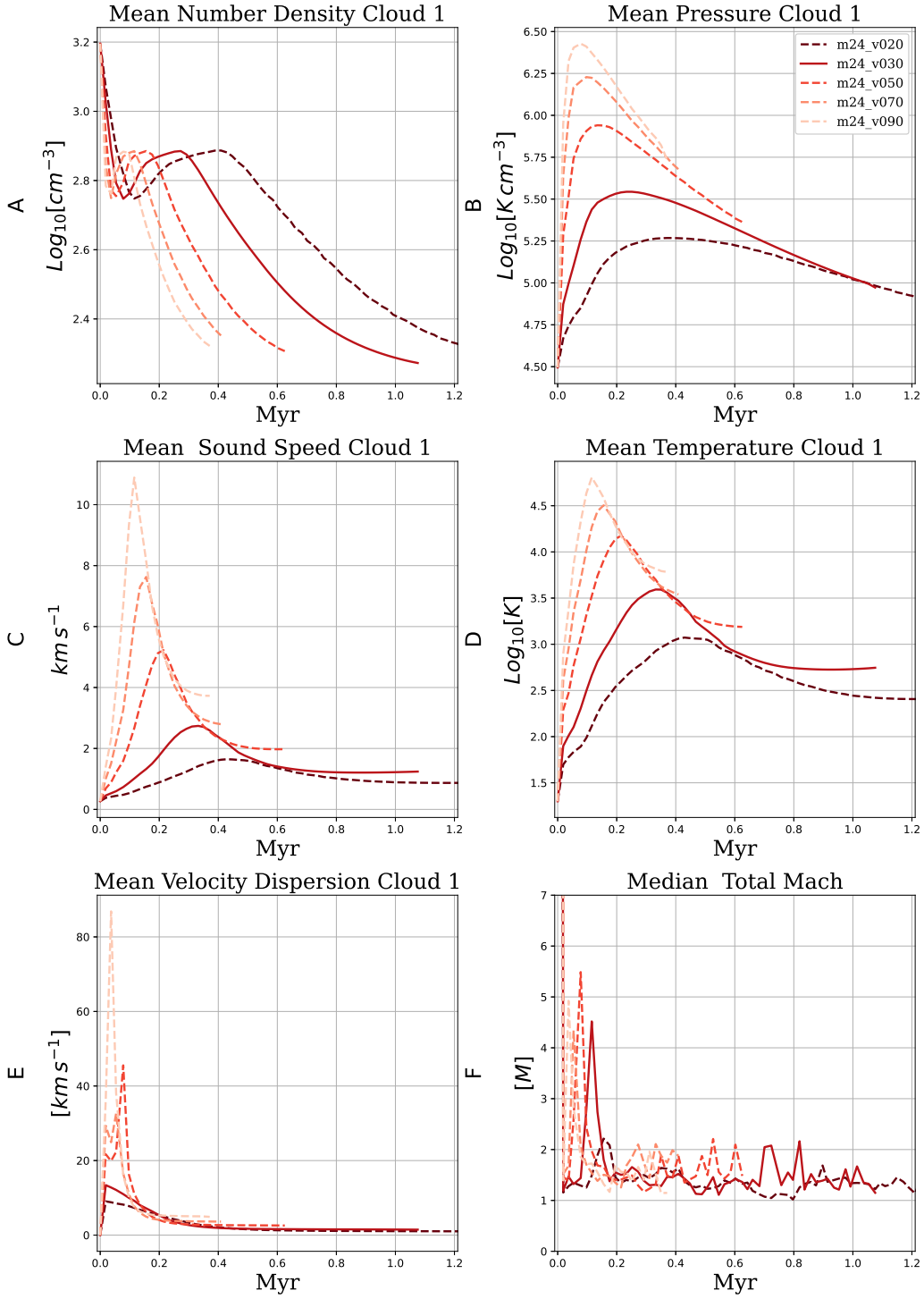


Figure 4.8: Diagnostic curves of the moving cloud for different collision velocities. Labels are presented on the corner of each panel, where the standard model is present in a solid line, with a collision velocity of 30 km s⁻¹ while models with a collision velocity of 20, 50, 70, 90 km s⁻¹ are presented in color decreasing color gradient in dashed lines. Panel B shows the labels for each velocity.

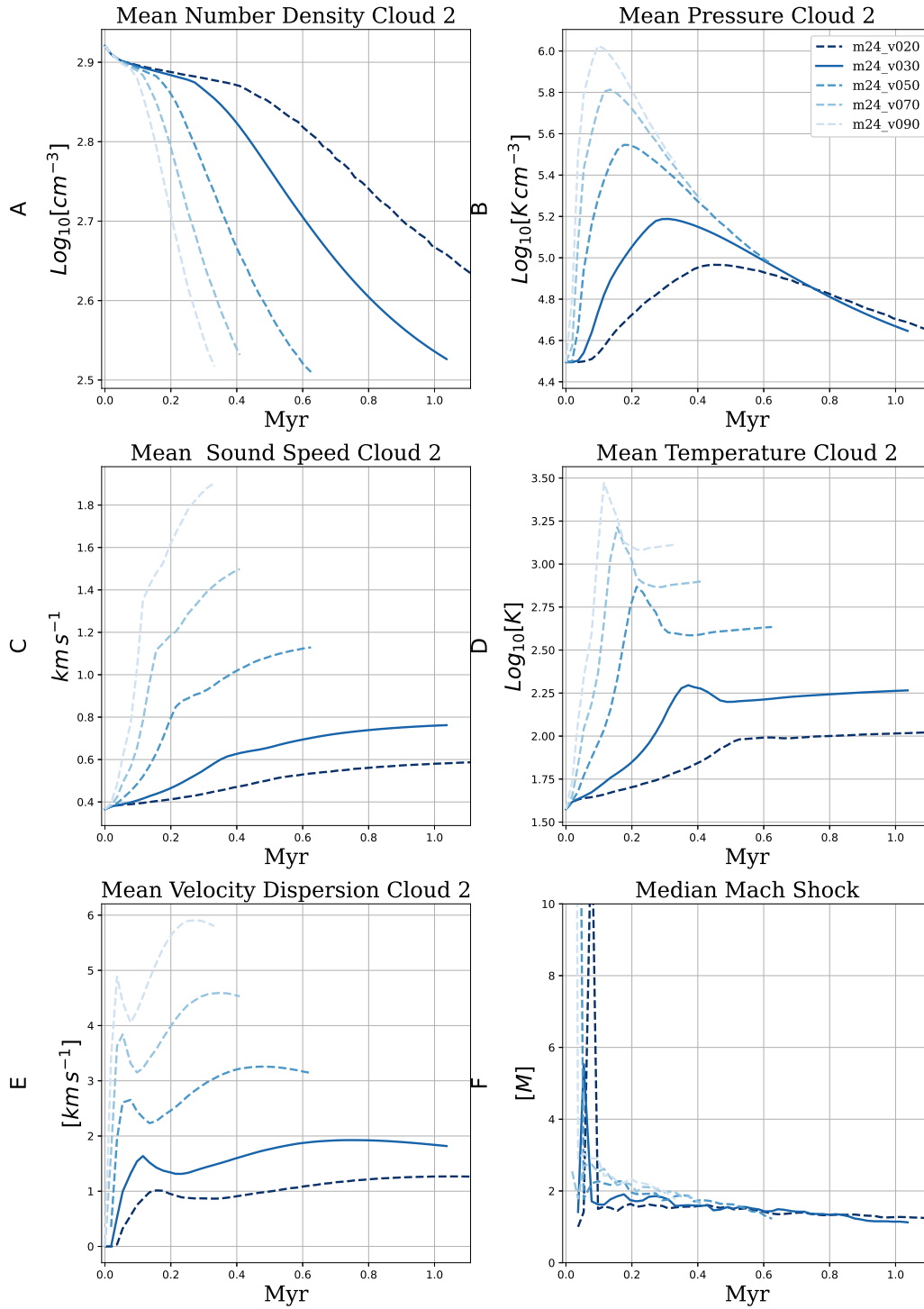


Figure 4.9: Diagnostic curves of the initially non-moving cloud for different collision velocities. Labels are presented on the top right panel, where the standard model is present in solid blue lines, with a collision velocity of 30 km s^{-1} while models with a collision velocity of $20, 50, 70, 90 \text{ km s}^{-1}$ are presented in color decreasing color gradient in dashed lines. Panel B shows the labels for each velocity.

The initial decreasing trend is a product of the cloud's motion, creating high velocities and pressure differences. The second cloud presents different characteristics because it has a strong shock as the velocity increases, given a median of $M \approx 8$, which suggests a very energetic collision at the initial stages after which both clouds converge to a characteristic shock Mach number $M \approx 1,5$

4.4. Evolution of shock the shock distribution

In this section, we discuss the results that we obtain by using our shock-finding algorithm and Python code to detect and characterize perturbations in the CCc models. To illustrate some of the intermediate state of steps of our shock-finding routine, Figures 4.10 and 4.11 present different maps with snapshots of the velocity divergence and the pressure gradient at different periods of the collision evolution. These maps help us to tag the candidate shock cells, as was mentioned in 3.3 and 2.2, where we describe the step-by-step method employed by our algorithm for detecting shocks. In the case of the velocity divergence, the maps show the locations where the convergent flow exists. Notice that at time $t = 0Myr$, there is a discontinuity because the moving cloud has an initial velocity. We can see that most of them are in the front and in the tail of the collision. This can be noticed in the first stage of the collision (first 2 rows), where gas compression creates high-density regions that move against the background gas. On the other hand, at the back of the cloud, convergence flow emerges from reflected waves enveloping the moving cloud and following across the rarefaction zone. This effect is more evident in the first two stages of the simulation. The formation of the bow shock is evident in the front of the collisions. The importance of the velocity divergence is that it gives an idea of the distribution of the regions where shocked gas exists. As was mentioned in Chapter 2 and 3, sudden changes in gas velocities across the grid suggest the presence of shock waves as they are characterized by the strong compression exerted by the kinetic energy of the moving cloud. Velocity divergence maps can be complemented by information coming from the pressure gradient. As we saw in Chapter 2, shocks also create large pressure gradients. The pressure gradient maps (Figure 4.11) also give information about candidate shocked cells. Because the difference in the pressure of continuous cells may vary a lot between the shock front and the unperturbed cell, this difference is characterized as an abrupt change in the pressure gradient on a small region. Shocked gas in the post-shock flows has a huge pressure compared with the unperturbed pre-shock region, which has a lower pressure. This difference in pressure guarantees the propagation of the shock in the direction of the small pressure. Additionally, the pressure gradient provides the location where the physical properties of the gas have changed because of shock, which transforms the kinetic energy of the colliding cloud into thermal energy. This means that the collision has the capacity to heat up the gas, increasing the temperature and pressure. Figure 4.11 only shows the most evident shock and high-pressure gradients, namely bow shock and the initial interaction of the colliding clouds.

Figure 4.12 shows the final maps of the shocked gas (which takes both the velocity divergence and pressure gradients into account. See Section 2.2). These maps show shock Mach numbers at different times in the standard model ($m24_v030$ see table 3.2.5). Clearly, we can see the presence of strong shocks in the front of the collisions, also known as bow shock. At the initial stage where the collision starts, the clouds interact, and the compression of the cloud-cloud boundary layers appears, creating strong shocks with high Mach numbers in this region. Also, there

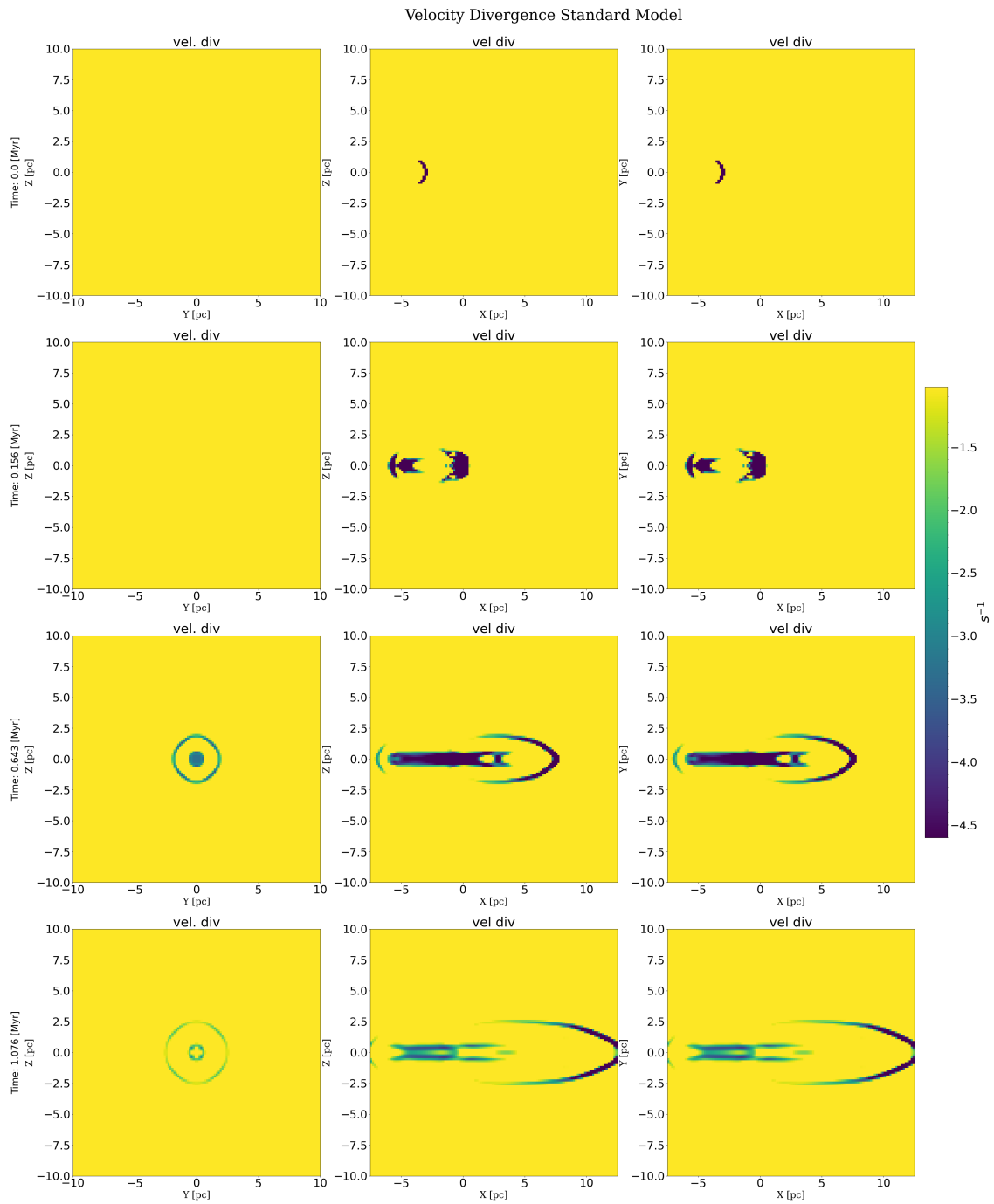


Figura 4.10: Maps of 2D slices at X=0, Y=0 and Z=0 of velocity divergence in the standard model (*m24_v030* see table 3.2.5). Discontinuity zones are depicted in these maps.

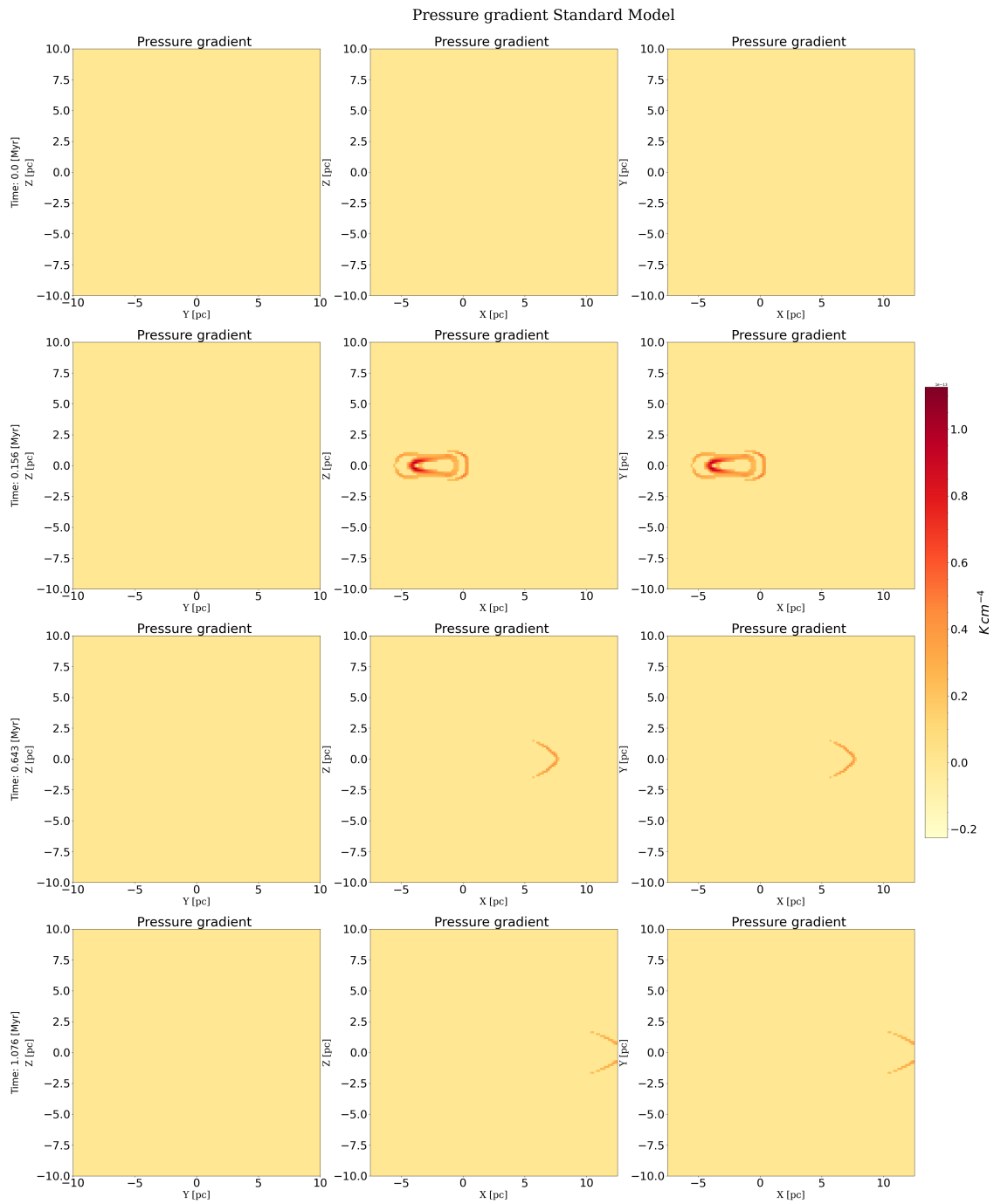


Figure 4.11: Maps of 2D slices at $X = 2.5$, $Y = 0$ and $Z = 0$ of pressure gradient in the standard model ($m24_v030$ see table 3.2.5). Discontinuity zones are depicted in these maps.

are secondary boundaries with the same form as the bow shock but with less intensity near the front of the collision, which likely has a geometrical origin as clouds are spherical. Additionally, another region where shocks appear in the back end of the rarefaction region where low-pressure regions are surrounded by the higher-pressure ambient gas.

Figure 4.12 also reveals the formation of the Mach cone. The Mach cone's appearance is a direct effect of the supersonic motion of the moving cloud as it moves through the initially non-moving cloud. The supersonic motion creates shock waves that move in the opposite direction with respect to the cloud trajectory. This is created by the motion of the cloud. Thus affecting the gas inside of the first cloud. The shock waves form a conical pattern influenced by the Mach number, which controls the angle of the cone.

The third row in Figure 4.12 shows the evolution of the collision and the interaction between the bow shock and the second front, which together create internal shocks in the middle of these two regions. This is a result of reflected waves traveling inwards from the borders, but we would also expect additional contributions from instabilities that can be present in this kind of simulation, such as the *Kelvin-Helmholtz* or the *Rayleigh-Taylor* instabilities. Also, in the 2 last rows of Figure 4.12, the two fronts merge into one, and it has instabilities at the borders. Looking into the rarefaction zone, the presence of the Mach cone is more evident. The angle of the Mach cone is narrower at the back of this region.

4.4.1. Time evolution of shock Mach numbers

To complement the analysis above, we now discuss how the population of shocks changes with time in CCc models. Figure 4.13 shows the evolution of the distribution of the shock Mach numbers over time. This corresponds to the standard model where higher Mach numbers occur at the beginning of the simulation. This happens as a result of the interaction of the cloud with the ambient medium produced by the motion of the cloud. Notice that as the simulation evolves, the shock Mach number and the number of shocked cells start to decrease slowly to Mach number around $M \sim 4$. Mach numbers around these values are characteristic values for observed CCc regions in the ISM, which we presented in Chapter 1. The different colors in the figure present different times in the evolution of the collision. The number of strong shocked cells decreases as time evolves, and the distribution of the shock waves moves slowly to the left. Clearly, most of the perturbed cells in our simulation are subsonic waves, so dissipation is ultimately controlled by energy dissipation in turbulent eddies rather than at shocks (which is in agreement with studies on ISM turbulence, see Federrath *et al.* (2009)).

Despite this, there are also very strong shocks produced by the collisions, so we also isolate shock Mach numbers in our analysis. Only shock waves are presented in the right panel of Figure 4.13, which we can analyze in more detail. All of the histograms indicate similar trends and that most of the shocked cells have low Mach numbers. As time evolves, the number of cells with low Mach number values increases due to dissipation. Thermal energy is quickly lost at strong shocks.

In addition, we also analyze the shock populations in each of the clouds individually. Figures 4.14 and 4.15 show the distribution of Mach numbers at different times for the moving cloud and the initially non-moving cloud, respectively. The main characteristic exhibited by both clouds is the large amount of subsonic waves present in them,

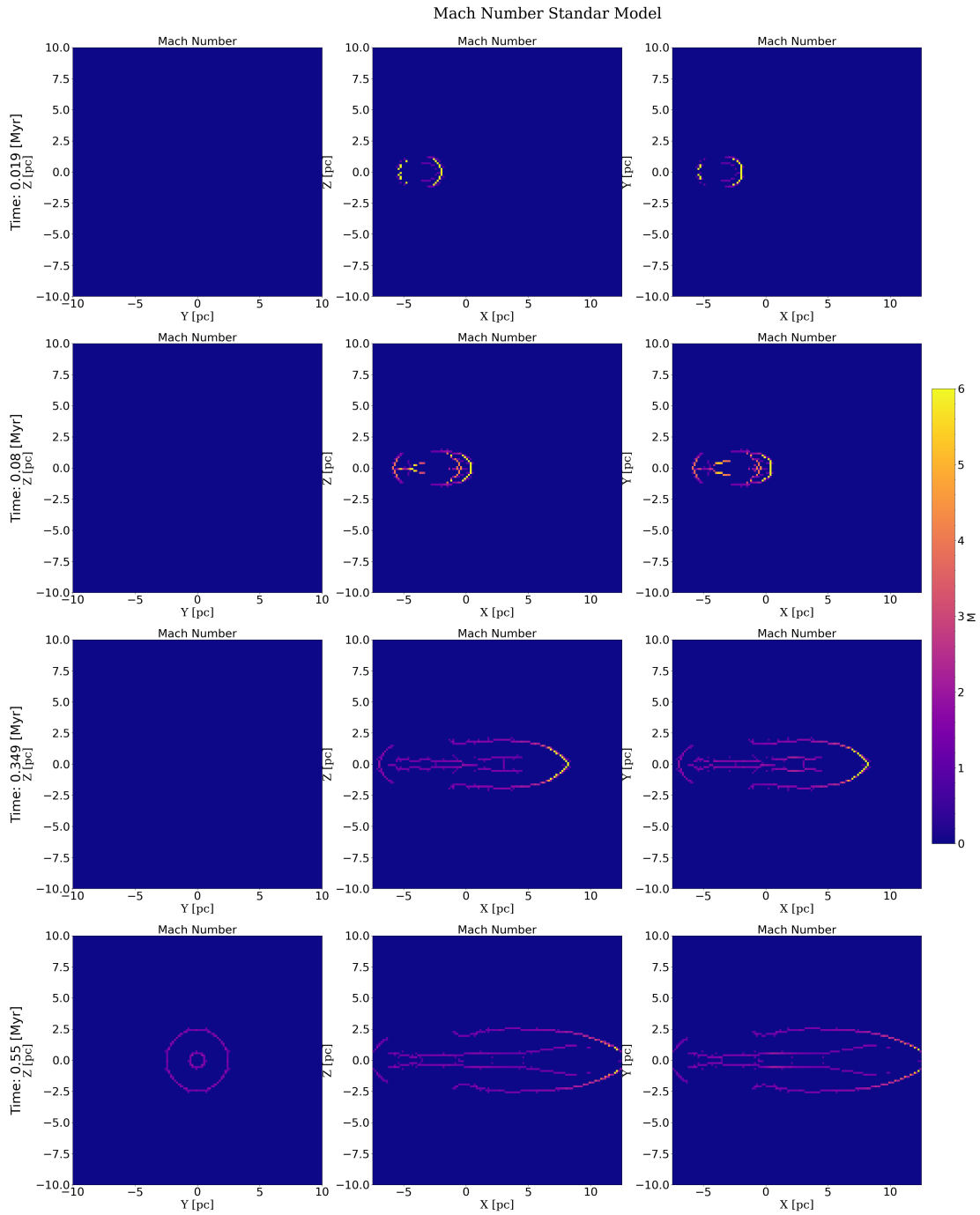


Figure 4.12: Maps of 2D slices at $X = 2.5$, $Y = 0$, and $Z = 0$ of the shock Mach numbers in the standard model ($m24_v030$ see table 3.2.5). Shocks are shown in brighter colors.

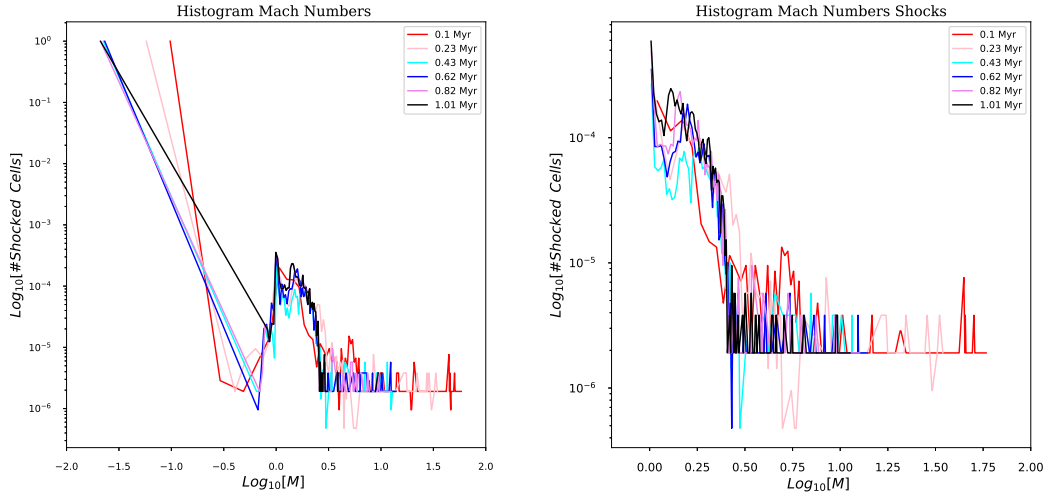


Figure 4.13: Histograms showing the Mach numbers of all of the subsonic and supersonic perturbations (left) and only of supersonic shocks (right) in our standard CCc (model *m24_v030*).

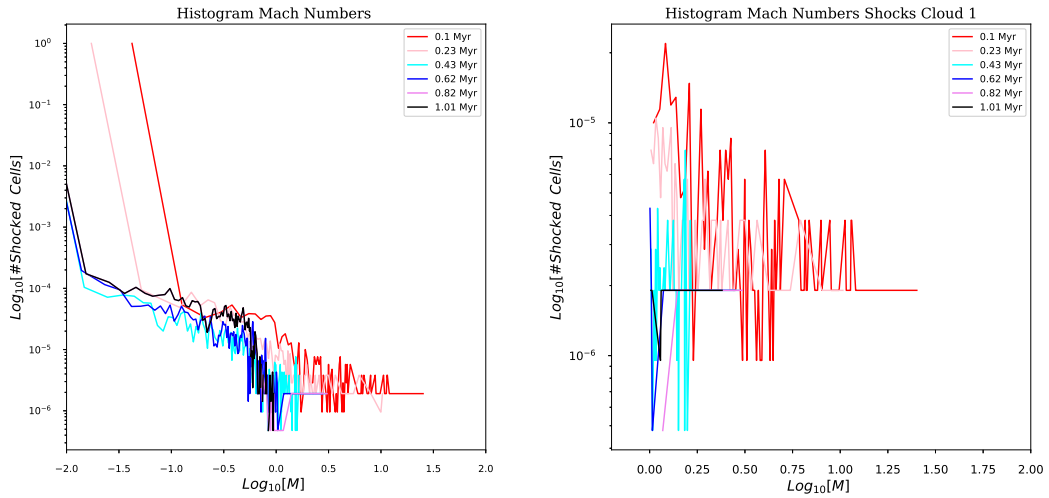


Figure 4.14: Histograms showing the Mach numbers for the moving cloud of all of the subsonic and supersonic perturbations (left) and only of supersonic shocks (right) in our standard CCc (model *m24_v030*).

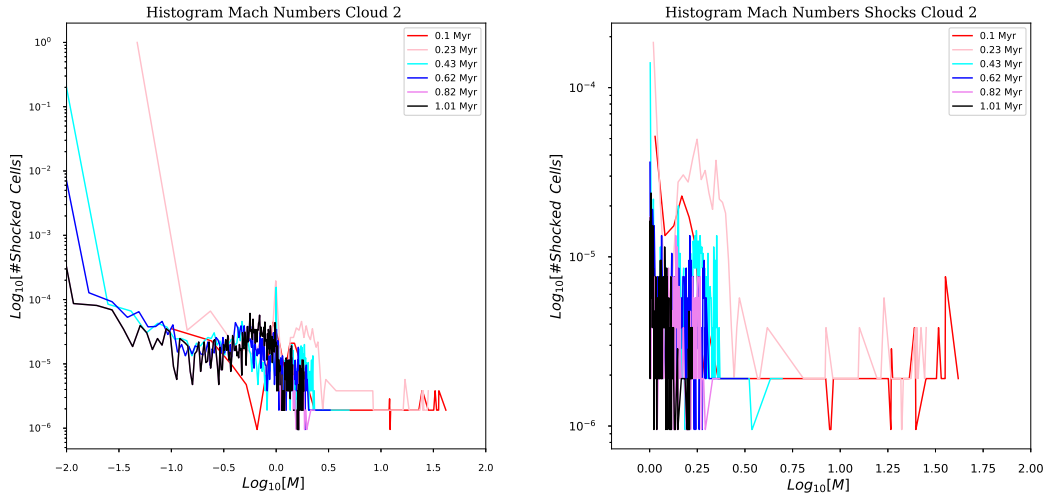


Figure 4.15: Histograms showing the Mach numbers for the initially non-moving cloud of all of the subsonic and supersonic perturbations (left) and only of supersonic shocks (right) in our standard CCc (model *m24_v030*).

but there is a small difference between these two clouds. At the beginning of the collisions, the initially non-moving cloud does not contain as many subsonic waves compared with the first moving cloud. This indicates that subsonic waves are predominantly produced by shear flows inside moving gas. Also, the initially non-moving cloud (see Figure 4.14) presents more shocked cells all the time as shocks can readily form and propagate across the larger volume of the initially non-moving cloud. But as time progresses, the number of shocked cells decreases substantially for the colliding cloud 4.15 for times near to 1 Myr because of the thermal dissipation.

Capítulo 5

Conclusions & Outlook

The evolution of the interstellar medium (ISM) comprises several dynamical processes. One of such processes is the collisions of ISM clouds, which can trigger star formation. Cloud-cloud collisions have been studied observationally and theoretically before and are used to explain star formation regions in our Galaxy. However, simulations varying the cloud sizes and the collision velocities have not been performed. This thesis studies and discusses the influence of the size of the colliding clouds and the collision velocities on the evolution and shock distributions of cloud-cloud collisions, in which clouds satisfy Larson's laws. This research was performed by using hydrodynamical simulation and our own Python post-processing routines :

- We successfully ran a set of hydrodynamical simulations using the PLUTO code and varying the initial conditions, such as the cloud size and the collision velocity. We vary the collision velocities from typical values of CCc simulation, such as 20km s^{-1} , to high collision velocity ($> 50\text{km s}^{-1}$), which cannot be explored yet. Our simulation of changing the cloud size corroborates the previous work for an identical cloud model.
- We developed a Python shock-finding routine based on an algorithm that uses the Rankine-Hugoniot jump conditions and particularly the so-called velocity jump (VJ) method, which relies on searching for convergent flows and large pressure gradients to find shocks (see Chapter 2). Our algorithm successfully detects shocked cells and classifies them into subsonic waves and shocks. The algorithms work efficiently in all our simulations.
- The evolution of cloud-cloud collisions can be separated into three different stages.: 1) **Compressing stage**. The moving cloud approaches the initially non-moving larger cloud and starts to compress the material inside the larger cloud creating a U cavity. 2) **Pass-through stage**. The material of the colliding cloud has passed through the whole length of the cloud and promotes the formation of the Mach cone as convergence flows meet at the back of the moving cloud. 3) **Dissipation stage**. All the material of the larger initially non-moving cloud has been affected by the collision, and the dissipation process changes from being controlled by shocks to turbulent eddies (see Section 4.1).
- Varying the size of the colliding cloud has a direct effect on the cross-section, which is larger for the identical

cloud model. In the standard model, the physical properties of the moving cloud are more affected given that the initially non-moving cloud is larger and surrounds it, while for the identical cloud model, the initially non-moving cloud is more affected due to the larger cross-section, and both clouds are efficiently destroyed (see Section 4.2).

- The identical cloud model collision between two clouds of the same size produces stronger shocks in both clouds compared with the standard model, especially for the initially non-moving cloud where most of the shocks are present (see Section 4.2).
- Changes in the collision velocities exhibit a scaling effect in time where the integrated quantities in all the models are similar and just appear shifted in time. Despite this, the actual intensity of the lines is correlated with the collision velocity. For example, there was an increase in pressure as we increased the velocity. Increments in collision velocity also create stronger rarefaction zones for higher velocities as revealed by the motion of the moving cloud, which leaves behind low densities (see Section 4.3).
- The collision velocity can increase the temperature. For high-velocity collisions with $v > 50 \text{ km s}^{-1}$, the moving cloud even reached the temperature conditions that are optimal to ionize the gas. Instead, for the low-velocity models, the reached temperatures suggest that most of the gas either remains molecular or becomes cold neutral gas (see Section 4.3).
- In terms of the shock population analysis, the median Mach number also exhibits scaling effects with increasing collision velocities as the distribution moves to earlier times for higher collision velocities. However, this effect is only present in the second cloud, initially non-moving, where high-velocity collisions shows high values of shock Mach numbers.
- We also find that our initially non-moving cloud remains supersonic during the whole simulation while the colliding (moving) cloud changes its turbulence regime from supersonic to subsonic and returns again to supersonic during the time when it interacts with the initially non-moving cloud (see Section 4.4).
- Shock cells were detected and tagged by our algorithm which effectively searches for convergence flows and high-pressure gradients. Our Python code outputs all the shocked cells. Our simulation shows that shocks form predominantly in two regions: the bow shock in front of the moving cloud and the Mach cone at the rear of both clouds (see Section 4.4).
- The shock distribution shows that most of the perturbations created by the collisions are subsonic waves, even though there are considerable numbers of shocks too. The shock distribution show a very characteristic displacement to the lower shock Mach number values as time evolves and dissipation processes migrate from shock dissipation to turbulent eddy dissipation. At the beginning of the collisions, there are strong shocks that start to lose energy quickly, but as time evolves most shocks turn into subsonic waves. Most of the shocks have $M \sim 3$, a characteristic value of the star formation regions, potentially triggered by CCs, that are observed in the ISM of our Galaxy (see Section 4.4).

Overall our algorithm is robust for shock detection for different models. Changes in the initial conditions of the cloud directly affect the amount of shocked cells and the strength of the shocks. Future work should increase the resolution of the Cc simulation to understand the dissipation process, instabilities, and additionally add other physical such as self-gravity, turbulence, and magnetic fields. It would be also interesting to collide fractal clouds for more realistic simulations. On the technical side, we also suggest enlarging the computational domain to prevent mass losses from biasing the results.

Apéndice A

Normalization units

For introducing dimensions, we use the normalization units from the grid.out file and derived the other related quantities.

- $[\rho_0] = 3,841 \times 10^{-21} \text{ g cm}^{-3}$
- $[v_0] = 5 \times 10^5 \text{ cm} = 5 \text{ km}$
- $[P_0] = 9,6025 \times 10^{-10} \text{ dyn cm}^{-2} = 6,154855 \times 10^6 \text{ K cm}^{-3}$
- $[L_0] = 3,086 \times 10^{19} \text{ cm} = 10,001 \text{ pc}$
- $[m_0] = 1,1288 \times 10^{38} \text{ g} = 5,675411 \times 10^4 M_\odot$
- $[t_0] = 6,172 \times 10^{13} \text{ s} = 1,9592 \text{ Myr}$
- $[T_0] = \frac{m\mu}{K_b} v_0^2 = 7,0958 \times 10^3 \text{ K}$

In the last item, m is the atomic unit, and $\mu = 2,36$ for all simulations. We used the normalization units to assign dimensions to our simulation. We multiplied the above quantities by the different 3D arrays containing data information.

Bibliography

- [1] Fukui, Y.; Habe, A.; Inoue, T.; Enokiya, R.; Tachihara, K. Cloud–cloud collisions and triggered star formation. *Publications of the Astronomical Society of Japan* **2021**, *73*, S1–S34.
- [2] Armijos-Abendaño, J.; Banda-Barragán, W.; Martín-Pintado, J.; Dénes, H.; Federrath, C.; Requena-Torres, M. A. Structure and kinematics of shocked gas in Sgr B2: further evidence of a cloud–cloud collision from SiO emission maps. *Monthly Notices of the Royal Astronomical Society* **2020**, *499*, 4918–4939.
- [3] Zeng, S.; Zhang, Q.; Jiménez-Serra, I.; Tercero, B.; Lu, X.; Martín-Pintado, J.; De Vicente, P.; Rivilla, V.; Li, S. Cloud–cloud collision as drivers of the chemical complexity in Galactic Centre molecular clouds. *Monthly Notices of the Royal Astronomical Society* **2020**, *497*, 4896–4909.
- [4] Nieva, M.-F.; Przybilla, N. Present-day cosmic abundances-A comprehensive study of nearby early B-type stars and implications for stellar and Galactic evolution and interstellar dust models. *Astronomy & Astrophysics* **2012**, *539*, A143.
- [5] Chevance, M.; Kruijssen, J. D.; Hygate, A. P.; Schrubba, A.; Longmore, S. N.; Groves, B.; Henshaw, J. D.; Herrera, C. N.; Hughes, A.; Jeffreson, S. M. The lifecycle of molecular clouds in nearby star-forming disc galaxies. *Monthly Notices of the Royal Astronomical Society* **2020**, *493*, 2872–2909.
- [6] Saintonge, A.; Catinella, B. The Cold Interstellar Medium of Galaxies in the Local Universe. *Annual Review of Astronomy and Astrophysics* **2022**,
- [7] Delgado, R. G.; García-Benito, R.; Pérez, E.; Fernandes, R. C.; De Amorim, A.; Cortijo-Ferrero, C.; Lacerda, E.; Fernández, R. L.; Vale-Asari, N.; Sánchez, S. F. The CALIFA survey across the Hubble sequence-Spatially resolved stellar population properties in galaxies. *Astronomy & Astrophysics* **2015**, *581*, A103.
- [8] Botticella, M.; Smartt, S.; Kennicutt, R.; Cappellaro, E.; Sereno, M.; Lee, J. A comparison between star formation rate diagnostics and rate of core collapse supernovae within 11 Mpc. *Astronomy & Astrophysics* **2012**, *537*, A132.
- [9] McKee, C. F.; Ostriker, E. C. Theory of star formation. *Annu. Rev. Astron. Astrophys.* **2007**, *45*, 565–687.

- [10] Gnedin, N. Y.; Glover, S. C.; Klessen, R. S.; Springel, V.; Klessen, R. S.; Glover, S. C. Physical processes in the interstellar medium. *Star Formation in Galaxy Evolution: Connecting Numerical Models to Reality: Saas-Fee Advanced Course 43. Swiss Society for Astrophysics and Astronomy* **2016**, 85–249.
- [11] Miura, H.; Yamamoto, T.; Nomura, H.; Nakamoto, T.; Tanaka, K. K.; Tanaka, H.; Nagasawa, M. Comprehensive study of thermal desorption of grain-surface species by accretion shocks around protostars. *The Astrophysical Journal* **2017**, 839, 47.
- [12] Hollenbach, D.; McKee, C. F. Molecule formation and infrared emission in fast interstellar shocks. I Physical processes. *Astrophysical Journal Supplement Series*, vol. 41, Nov. 1979, p. 555–592. **1979**, 41, 555–592.
- [13] Vidali, G. H₂ formation on interstellar grains. *Chemical reviews* **2013**, 113, 8762–8782.
- [14] Butsky, I. S.; Fielding, D. B.; Hayward, C. C.; Hummels, C. B.; Quinn, T. R.; Werk, J. K. The impact of cosmic rays on thermal instability in the circumgalactic medium. *The Astrophysical Journal* **2020**, 903, 77.
- [15] Simpson, C. M.; Pakmor, R.; Pfrommer, C.; Glover, S. C.; Smith, R. How cosmic rays mediate the evolution of the interstellar medium. *Monthly Notices of the Royal Astronomical Society* **2023**, 520, 4621–4645.
- [16] Padovani, M.; Hennebelle, P.; Marcowith, A.; Ferrière, K. Cosmic-ray acceleration in young protostars. *Astronomy & Astrophysics* **2015**, 582, L13.
- [17] Commerçon, B.; Marcowith, A.; Dubois, Y. Cosmic-ray propagation in the bi-stable interstellar medium-I. Conditions for cosmic-ray trapping. *Astronomy & Astrophysics* **2019**, 622, A143.
- [18] Compiègne, M.; Verstraete, L.; Jones, A.; Bernard, J.-P.; Boulanger, F.; Flagey, N.; Le Bourlot, J.; Paradis, D.; Ysard, N. The global dust SED: tracing the nature and evolution of dust with DustEM. *Astronomy & Astrophysics* **2011**, 525, A103.
- [19] Hotokezaka, K.; Kiuchi, K.; Shibata, M.; Nakar, E.; Piran, T. Synchrotron radiation from the fast tail of dynamical ejecta of neutron star mergers. *The Astrophysical Journal* **2018**, 867, 95.
- [20] Schlickeiser, R. Nonthermal radiation from jets of active galactic nuclei: Electrostatic bremsstrahlung as alternative to synchrotron radiation. *Astronomy & Astrophysics* **2003**, 410, 397–414.
- [21] Frau, P.; Galli, D.; Girart, J. M. Comparing star formation models with interferometric observations of the protostar NGC 1333 IRAS 4A-I. Magnetohydrodynamic collapse models. *Astronomy & Astrophysics* **2011**, 535, A44.
- [22] Reissl, S.; Wolf, S.; Seifried, D. Tracing the ISM magnetic field morphology: the potential of multi-wavelength polarization measurements. *Astronomy & Astrophysics* **2014**, 566, A65.
- [23] Tacconi, L. J.; Genzel, R.; Sternberg, A. The evolution of the star-forming interstellar medium across cosmic time. *Annual Review of Astronomy and Astrophysics* **2020**, 58, 157–203.

- [24] Wadekar, D.; Wang, Z. Constraining axion and compact dark matter with interstellar medium heating. *Physical Review D* **2023**, *107*, 083011.
- [25] Kalashnikov, I. Y.; Chechetkin, V. Influence of dark matter on gravitational stability of isothermal gas clouds. *Monthly Notices of the Royal Astronomical Society* **2022**, *514*, 1351–1358.
- [26] Langer, W.; Pineda, J.; Goldsmith, P.; Chambers, E.; Riquelme, D.; Anderson, L.; Luisi, M.; Justen, M.; Buchbender, C. The dense warm ionized medium in the inner Galaxy. *Astronomy & Astrophysics* **2021**, *651*, A59.
- [27] Draine, B. T. *Physics of the interstellar and intergalactic medium*; Princeton University Press, 2010; Vol. 19.
- [28] Xu, S.; Zhang, B. Scatter broadening of pulsars and implications on the interstellar medium turbulence. *The Astrophysical Journal* **2017**, *835*, 2.
- [29] Falceta-Gonçalves, D.; Kowal, G.; Falgarone, E.; Chian, A.-L. Turbulence in the interstellar medium. *Nonlinear Processes in Geophysics* **2014**, *21*, 587–604.
- [30] Burkhart, B.; Lazarian, A.; Goodman, A.; Rosolowsky, E. Hierarchical structure of magnetohydrodynamic turbulence in position-position-velocity space. *The Astrophysical Journal* **2013**, *770*, 141.
- [31] Yun, H.-S.; Lee, J.-E.; Evans II, N. J.; Offner, S. S.; Heyer, M. H.; Cho, J.; Gaches, B. A.; Yang, Y.-L.; Chen, H.-H.; Choi, Y. TIMES II: Investigating the Relation Between Turbulence and Star-forming Environments in Molecular Clouds. *arXiv preprint arXiv:2107.13323* **2021**,
- [32] Cortes, P.; Parra, R.; Cortes, J.; Hardy, E. G30. 79 FIR 10: a gravitationally bound infalling high-mass star-forming clump. *Astronomy & Astrophysics* **2010**, *519*, A35.
- [33] Monaci, M.; Magnani, L.; Shore, S. N.; Olofsson, H.; Joy, M. R. Shear, writhe and filaments: turbulence in the high latitude molecular cloud MBM 40. *arXiv preprint arXiv:2306.06670* **2023**,
- [34] Saito, T.; Iono, D.; Espada, D.; Nakanishi, K.; Ueda, J.; Sugai, H.; Yun, M. S.; Takano, S.; Imanishi, M.; Miyama, T. Spatially Resolved Dense Molecular Gas Excitation in the Nearby LIRG VV 114. *The Astrophysical Journal* **2018**, *863*, 129.
- [35] Woodward, P. R. Theoretical models of star formation. *Annual Review of Astronomy and Astrophysics* **1978**, *16*, 555–584.
- [36] Inoue, T.; Fukui, Y. Formation of massive molecular cloud cores by cloud–cloud collision. *The Astrophysical Journal Letters* **2013**, *774*, L31.
- [37] Stone, M. E. Collisions Between H I Clouds. I. One-Dimensional Model. *Astrophysical Journal*, vol. 159, p. 277 **1970**, *159*, 277.

- [38] Takahira, K.; Tasker, E. J.; Habe, A. DO CLOUD–CLOUD COLLISIONS TRIGGER HIGH-MASS STAR FORMATION? I. SMALL CLOUD COLLISIONS. *The Astrophysical Journal* **2014**, 792, 63.
- [39] Torii, K.; Hasegawa, K.; Hattori, Y.; Sano, H.; Ohama, A.; Yamamoto, H.; Tachihara, K.; Soga, S.; Shimizu, S.; Okuda, T. CLOUD–CLOUD COLLISION AS A TRIGGER OF THE HIGH-MASS STAR FORMATION: A MOLECULAR LINE STUDY IN RCW 120. *The Astrophysical Journal* **2015**, 806, 7.
- [40] Torii, K.; Hattori, Y.; Hasegawa, K.; Ohama, A.; Haworth, T. J.; Shima, K.; Habe, A.; Tachihara, K.; Mizuno, N.; Onishi, T. Triggered O Star Formation in M20 via Cloud–Cloud Collision: Comparisons between High-resolution CO Observations and Simulations. *The Astrophysical Journal* **2017**, 835, 142.
- [41] Balfour, S.; Whitworth, A.; Hubber, D.; Jaffa, S. Star formation triggered by cloud–cloud collisions. *Monthly Notices of the Royal Astronomical Society* **2015**, 453, 2471–2479.
- [42] Haworth, T.; Tasker, E.; Fukui, Y.; Torii, K.; Dale, J.; Shima, K.; Takahira, K.; Habe, A.; Hasegawa, K. Isolating signatures of major cloud–cloud collisions using position–velocity diagrams. *Monthly Notices of the Royal Astronomical Society* **2015**, 450, 10–20.
- [43] Patra, S.; Evans II, N. J.; Kim, K.-T.; Heyer, M.; Kauffmann, J.; Jose, J.; Samal, M. R.; Das, S. R. Tracers of Dense Gas in the Outer Galaxy. *The Astronomical Journal* **2022**, 164, 129.
- [44] Harris, A.; Baker, A.; Zonak, S.; Sharon, C.; Genzel, R.; Rauch, K.; Watts, G.; Creager, R. CO J= 1–0 SPECTROSCOPY OF FOUR SUBMILLIMETER GALAXIES WITH THE ZPECTROMETER ON THE GREEN BANK TELESCOPE. *The Astrophysical Journal* **2010**, 723, 1139.
- [45] Pety, J.; Guzmán, V. V.; Orkisz, J. H.; Liszt, H. S.; Gerin, M.; Bron, E.; Bardeau, S.; Goicoechea, J. R.; Gratier, P.; Le Petit, F. The anatomy of the Orion B giant molecular cloud: A local template for studies of nearby galaxies. *Astronomy & Astrophysics* **2017**, 599, A98.
- [46] Gallagher, M. J.; Leroy, A. K.; Bigiel, F.; Cormier, D.; Jiménez-Donaire, M. J.; Ostriker, E.; Usero, A.; Bolatto, A. D.; García-Burillo, S.; Hughes, A. Dense gas, dynamical equilibrium pressure, and star formation in nearby star-forming galaxies. *The Astrophysical Journal* **2018**, 858, 90.
- [47] Schinnerer, E.; Weiß, A.; Aalto, S.; Scoville, N. Multi-transition Study of M51’S Molecular Gas Spiral Arms. *The Astrophysical Journal* **2010**, 719, 1588.
- [48] Fukui, Y.; Torii, K.; Hattori, Y.; Nishimura, A.; Ohama, A.; Shimajiri, Y.; Shima, K.; Habe, A.; Sano, H.; Kohno, M. A New Look at the Molecular Gas in M42 and M43: Possible Evidence for Cloud–Cloud Collision that Triggered Formation of the OB Stars in the Orion Nebula Cluster. *The Astrophysical Journal* **2018**, 859, 166.
- [49] Ginsburg, A.; Bally, J.; Barnes, A.; Bastian, N.; Battersby, C.; Beuther, H.; Brogan, C.; Contreras, Y.; Corby, J.; Darling, J. Distributed star formation throughout the Galactic Center cloud Sgr B2. *The Astrophysical Journal* **2018**, 853, 171.

- [50] Sato, F.; Hasegawa, T.; Whiteoak, J. B.; Miyawaki, R. Cloud collision-induced star formation in sagittarius B2. I. Large-scale kinematics. *The Astrophysical Journal* **2000**, 535, 857.
- [51] Vazza, F.; Dolag, K.; Ryu, D.; Brunetti, G.; Gheller, C.; Kang, H.; Pfrommer, C. A comparison of cosmological codes: properties of thermal gas and shock waves in large-scale structures. *Monthly Notices of the Royal Astronomical Society* **2011**, 418, 960–985.
- [52] Lehmann, A.; Federrath, C.; Wardle, M. SHOCKFIND—an algorithm to identify magnetohydrodynamic shock waves in turbulent clouds. *Monthly Notices of the Royal Astronomical Society* **2016**, 463, 1026–1039.
- [53] Teutloff, F. Shock Waves in Magnetohydrodynamical Simulations of Galactic Wind-cloud Interactions. Ph.D. thesis, Universität Hamburg, 2021.
- [54] Mignone, A.; Bodo, G.; Massaglia, S.; Matsakos, T.; Tesileanu, O. e.; Zanni, C.; Ferrari, A. PLUTO: a numerical code for computational astrophysics. *The Astrophysical Journal Supplement Series* **2007**, 170, 228.
- [55] Sullivan, B.; Kaszynski, A. PyVista: 3D plotting and mesh analysis through a streamlined interface for the Visualization Toolkit (VTK). *Journal of Open Source Software* **2019**, 4, 1450.
- [56] Oliphant, T. E. *Guide to numpy*; Trelgol Publishing USA, 2006; Vol. 1.
- [57] McKinney, W. pandas: a foundational Python library for data analysis and statistics. *Python for high performance and scientific computing* **2011**, 14, 1–9.
- [58] Barrett, P.; Hunter, J.; Miller, J. T.; Hsu, J.-C.; Greenfield, P. matplotlib—A Portable Python Plotting Package. 2005.
- [59] Pohl, M.; Englmaier, P.; Bissantz, N. Three-dimensional distribution of molecular gas in the barred Milky Way. *The Astrophysical Journal* **2008**, 677, 283.
- [60] Schuller, F.; Csengeri, T.; Urquhart, J.; Duarte-Cabral, A.; Barnes, P.; Giannetti, A.; Hernandez, A.; Leurini, S.; Mattern, M.; Medina, S.-N. SEDIGISM: Structure, excitation, and dynamics of the inner Galactic interstellar medium. *Astronomy & Astrophysics* **2017**, 601, A124.
- [61] Takahira, K.; Shima, K.; Habe, A.; Tasker, E. J. Formation of massive, dense cores by cloud–cloud collisions. *Publications of the Astronomical Society of Japan* **2018**, 70, S58.
- [62] Higuchi, A. E.; Chibueze, J. O.; Habe, A.; Takahira, K.; Takano, S. ALMA VIEW OF G0. 253+ 0.016: CAN CLOUD–CLOUD COLLISION FORM THE CLOUD? *The Astronomical Journal* **2014**, 147, 141.
- [63] Barger, K. A.; Nidever, D. L.; Huey-You, C.; Lehner, N.; Rueff, K.; Freeman, P.; Birdwell, A.; Wakker, B. P.; Bland-Hawthorn, J.; Benjamin, R. Exploring hydrodynamic instabilities along the infalling high-velocity cloud complex A. *The Astrophysical Journal* **2020**, 902, 154.

- [64] Banda-Barragán, W.; Brügger, M.; Federrath, C.; Wagner, A. Y.; Scannapieco, E.; Cottle, J. Shock–multicloud interactions in galactic outflows–I. Cloud layers with lognormal density distributions. *Monthly Notices of the Royal Astronomical Society* **2020**, *499*, 2173–2195.
- [65] Federrath, C.; Klessen, R. S.; Schmidt, W. The fractal density structure in supersonic isothermal turbulence: solenoidal versus compressive energy injection. *The Astrophysical Journal* **2009**, *692*, 364.